# SYNTHESIS AND CHARACTERIZATION OF A NOVEL SENSOR FOR NITROAROMATIC MOLECULES

by

Andrei Nesmelov

A thesis submitted to the faculty of
The University of North Carolina at Charlotte
in partial fulfillment of the requirements
for the degree of Master of Science in
Chemistry

Charlotte

2019

Approved by:

_____
Dr. Thomas A. Schmedake

_____
Dr. Christopher Bejger

_____
Dr. Markus Etzkorn

_____
Dr. Valery Grdzelishvili

# ABSTRACT

ANDREI NESMELOV. Synthesis and Characterization of a Novel Sensor for Nitroaromatic Molecules (Under the direction of DR. THOMAS A. SCHMEDAKE)

New conjugated spirosilabifluorene networks have been synthesized and characterized. They exhibit high surface areas, negligible solubility, broad chemical stability, and bright fluorescence. The materials have been analyzed as potential sensors for nitroaromatic compounds. The fluorescence of the condensed networks is quenched in the presence of picric acid (1-hydroxy-2,4,6-trinitrobenzene), nitrobenzene, and other nitroaromatics. Stern-Volmer quenching studies indicate the quenching can be modeled accurately with adsorption isotherm models incorporating a surface binding affinity heterogeneity. Results show a significant sensitivity toward nitroaromatic compounds comparable to known literature, as well as an improvement in picric acid sensitivity.

# ACKNOWLEDGEMENTS

I would like to acknowledge Dr. Thomas A. Schmedake for giving me the opportunity and guidance to work on this project, as well as Dr. Christopher Bejger for allowing the use of his lab facilities. I would also like to acknowledge David Lee, who's research this project was built on. Finally, I would like to acknowledge Dr. Markus Etzkorn for his invaluable academic and administrative assistance, as well as the UNCC graduate school for the opportunity to participate in their master's program.

TABLE OF CONTENTS

# LIST OF TABLES

# LIST OF FIGURES

# LIST OF EQUATIONS

# LIST OF SCHEMES

# CHAPTER 1: INTRODUCTION

## 1.1 Overview of Porous Materials and Polymers

Recent developments in polymer science have focused on various forms of porous materials. Fundamentally, a porous material is simply a substrate which contains many voids, or pores. A simple example of this would be a solid foam. This can be generalized to any material in which a gas-solid interface is the dominant structural motif. Such materials have shown many unique chemical and physical properties.[4] Nanoporous materials in particular show promising applications in technological sectors such as transportation and logistics, renewable energy, construction, and biotechnology. The global market for such materials is rapidly increasing, with nearly 10% of modern polymer consumption intended for nanoporous materials. In the year 2019, the global production of porous polymers is expected to exceed 23 million tons.[4]

Porous polymeric materials have shown promise in materials development much like Bakelite, the first synthetic polymer, did in 1908. Bakelite began the polymer revolution due to its low cost, easy moldability, and resistance to electrical, chemical, and thermal degradation. Porous polymer systems improve upon this further, producing inherently lightweight and cheaper materials due to the reduction in total material mass. Further, the ability to copolymerize different monomers, as well as the physical structures that the polymers take, can be used to tune the properties of a material much further than can be done without nanoporous networks.[5]

Figure 1: Bakelite radio

Many natural materials exhibit nanoporosity. The classical example is a zeolite. Zeolites generally refer to hydrated aluminosilicates that have a three dimensional honeycomb structure.[6] These zeolites have shown use in many applications, including catalysis, gas absorption and sequestration, and adsorptive purification and filtration.[7-9] Hundreds of structures of zeolites, both natural and synthetic, have been identified.[10] Zeolites represent crystalline nanoporous materials, as they have an organized and repeating structure.

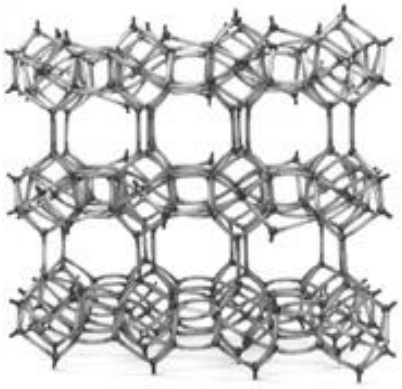

Figure 2: Zeolite structure displaying open pores

In addition to zeolites, various non-mineral nanoporous materials exist in nature. For example, bacterial cellulose, a nanoporous and crystalline cellulose structure formed by certain strains of bacteria.[11] These have shown promise in medical applications, shortening burn recovery time when compared to traditional silver-based treatments.[12] Finally, many biostructures can themselves be considered a form of nanoporous material due to their structure containing voids. Many biological membranes fall into this category of pseudo-porous structures, and well as heat shock protein aggregates.

Traditionally, zeolites were limited to catalytic roles in the petroleum industry, being used in the fluid catalytic cracking process to convert heavy gas oils into lighter gasoline fractions with higher octane ratings for consumer automobiles.[13] In the last few decades, however, zeolites have seen a surge of applications, from microelectronics to medical diagnosis.[14,15] This was caused in part by the ability to synthesize specific

zeolites with tunable properties. This allows the creation of specific zeolite morphologies. For example, highly polarized hydroxyl groups act as Bronsted acidic centers to catalyze the conversion of microbial lactic acid into lactide, which is a key feedstock in biodegradable polylactic acid.[16] Substituting silicon centers into the structure can, on the other hand, produce Lewis acid sites, such as those used in the production of biomass-derived terephthalic acid for the production of polyethylene terephthalate (PET).[17] Of course, these functionalities can be selectively combined for effective "one-pot" multistep reactions.[18] Zeolites are also used to immobilize other catalysts, such as noble metals, for composite catalysis.[19] The main drawbacks of zeolites right now are stability, product selectivity, and re-generatability.

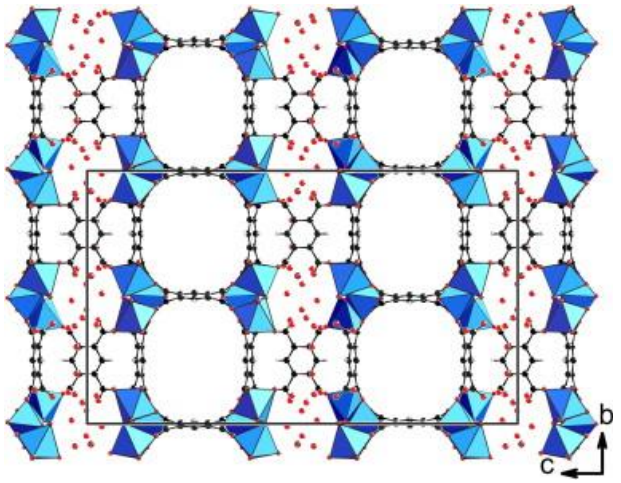

Figure 3: MOF-117[3]

Several synthetic organic porous polymers are also made. These are generally divided into a few different categories. The simplest division is whether they are crystalline or amorphous.[20] Crystalline polymer networks consist of ordered structures with uniform and predictable pore sizes. The pore size of a crystalline polymer network is directly related to the length of the monomer strut that makes up the polymer. Due to the thermodynamic stability of a crystalline network, crystalline polymers are generally formed from slow, reversible reactions. A classic example of a crystalline partially organic material would be Metal-Organic Frameworks, or MOFs.[21] Given the mixture of

organic spacers and metallic centers that make up a MOF structure, MOFs are very attractive materials for a large variety of tasks. They exhibit some of the highest porosity known to mankind, with surface areas in excess of 7000 $m^2g^{-1}$.[22] MOFs also have favorable properties much like zeolites, with the metal centers providing Lewis acidic locations for catalytic sites.[23] Additionally, MOFs show promise in energy storage applications as electrode materials for batteries, showing less wear than traditional cathodes and superior permeability to the porous carbon anode used in lithium ion batteries today.[21] However, MOFs struggle with chemical stability, some being air sensitive, and they are generally expensive and intensive to produce. This significantly limits the ability to use MOFs in many applications. Recent research has focused on the development of covalent organic frameworks, of COFs. COFs are crystalline networks of organic polymers. They are formed from slow, reversible reactions, normally in solvothermal conditions.[24] This allows the formation of a highly ordered, crystalline solid.[25] These materials usually have lower surface areas when compared to MOFs, due to the lack of large metal ions. However, the continuous organic polymer system does make them extremely stable while maintaining porosity.[26] The relative stability makes COFs an attractive prospect for gas storage applications, catalysis, and electron transport.[27]

Amorphous organic polymers can be further subdivided into several subgroups. The three main subgroups are distinguished primarily by their synthetic methods. Hypercrosslinked polymers (HCPs) are formed by adding crosslinking agents to previously formed polymer chains. This results in a relatively rigid polymer network with

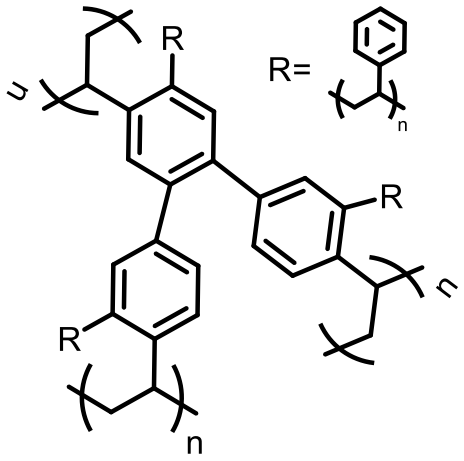


Figure 4: An example of hyper-crosslinked styrene.

very high porosity. When carried out in a solvothermal process, the stresses created by the solvation of the polymer forces links between multiple polymer chains, forming a relatively rigid three dimensional polymer network with porosity integrated into the structure itself.[28] Such HCPs are extremely effective for filtration applications, as the crosslinks can turn the polymer into a fairly dense, insoluble, material with low pore sizes.[29]

Another type of amorphous organic polymer is called a Conjugated Microporous Polymer (CMP). These polymers are defined by a continuous π-system along their backbone, allowing excellent electronic transfer along the polymer chain. These polymers have shown promise in electrochemical applications, as well as light-harvesting systems.[30] These show significant promise compared to current light harvesting methods, which commonly use expensive, scarce, and potentially toxic metal complexes ($Ru^{2+}$ and $Ir^{3+}$) and heterogenous semiconductors ($TiO_2$ and $Nb_2O_5$).[31] These polymers have an inherent porosity formed by the structure of the polymer and the rigid bonds between the monomers, which normally consist of one of more aryl rings, themselves. This usually results in stable nanopores and very high surface areas, while maintaining a π-conjugated

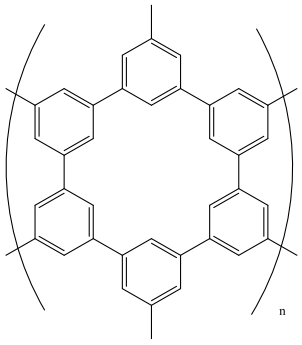


Figure 5: Simple conjugated polyphenyl polymer showing microporosity caused by rigid, conjugated, structure.

skeleton.[30] CMPs also benefit from the flexibility of the molecular building blocks themselves, as different monomers can be copolymerized together to form different macrostructures, as long as they maintain their conjugated backbone.[32]

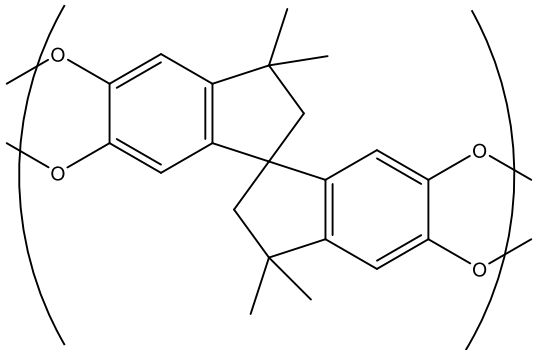


Figure 6: Polymer of Intrinsic Microporosity contorted around the spiro-carbon atom

The third type of amorphous organic polymer is a polymer of intrinsic microporosity, or PIMs. Intrinsic microporosity in polymers is defined as "a continuous network of interconnected intermolecular voids, which forms as a direct consequence of the shape and rigidity of the component macromolecules".[33] Unlike other polymers, where interactions between nearby polymer chains are enhanced and intermolecular void space is reduced, PIMs have overall more void volume. This is caused by a rigid fused ring structure centered on a central spiro-linkage, preventing free rotation.[33] The prevention of bond rotation can be achieved with either continuous fused rings or with extreme steric hindrance.[34] The rigid polymer backbone contorted around the spiro center prevents co-planar orientations, leading to high intermolecular free volume which is freely accessible to external molecular intercalation.[35] This leads to a solid material with a large proportion of interconnected free volume and very high surface areas.

Organic polymers have several advantages when compared to inorganic or organometallic compounds. First and foremost, they are generally less toxic. Second, they are generally much lighter, due to their constituent atoms, primarily C, H, O, and N,

being lightweight. Finally, organic polymers show very high chemical and thermal stability, compared to inorganic or organometallic polymers.[36] This is most readily apparent with MOFs, which are very sensitive to pH changes. Organic based polymers also benefit from the extensive developments in organic chemistry carried out through history, being much more varied. This synthetic diversity allows tuning the properties of a polymer much more carefully and intentionally when compared to less developed fields of chemistry.

PIMs also exhibit some favorable properties when compared to other porous organic polymers. PIMs can be solution processable, which is not possible for HCPs and CMPs. HCPs contain excessive and arbitrary crosslinks, which is inconsistent with any sort of reliable solubility. The rigid CMP backbone similarly prevents most attempts at solvation, which significantly limits the manufacturing possibilities of these polymeric systems. PIMs can also maintain porosity in wet chemical conditions, unlike, for example, boroxine based CMPs. Finally, unlike both CMPs and HCPs, which rely on either heterogenous monomer units or a secondary crosslinker addition respectively, PIMs have a chemical homogeneity which is seen as a great positive for certain applications.

As there is some overlap between the different types of polymers, we can combine several of these properties to create even more useful materials. For example, a PIM that has a fully conjugated backbone would take on the properties of a CMP, most notably electronic conduction as well as the ability to absorb radiation and emit fluorescence. This property can be increased further than small molecule optical absorption due to the delocalization of the charge throughout the polymeric structure.

This allows the tuning of specific emission frequencies which are otherwise difficult or impossible to achieve with small molecules. Combined with the high thermal and chemical stability inherent in organic PIMs, this allows for high efficiency fluorescence-based sensors. These sensors have been shown to follow well known Stern-Volmer relationships and can be very sensitive detectors for certain molecules that exhibit fluorescence quenching.

## 1.2 Spirobifluorenes

Spirobifluorene systems have recently become a focal point of polymer research, due to their favorable properties. In addition to their spiro-center, which precludes efficient packing, they have a high energy blue emission in the 400nm range, which makes them easily tunable fluorescence sensors for the entire visible spectrum. This is an attractive property, as it allows reliable sensing mechanisms that can be analyzed by the naked eye, instead of using instrumentation to detect emissions outside the visible spectrum[12]. As a result of this property, spirobifluorene systems are being investigated for many possible uses. In addition to fluorescence-based sensors, spirobifluorenes are of interest to OLED development, as one of the current problems with OLED-based displays is the lack of blue emitting compounds that are stable enough to not degrade within the expected display lifetime. This is usually assumed to be at least 10,000 hours.

## 1.3 Synthetic background

The synthesis of spirobifluorene systems is normally done through a condensation process between a fluorene and a 2,2’ substituted biphenyl molecule[37]. This results in a spiro-center. However, this synthetic method also has drawbacks. First, you cannot have substituents on the fluorene or the biphenyl that are more reactive than the substituents

that are forming the spiro center. This somewhat limits the flexibility of the spirobifluorene for future reaction. Second, substitution of the spirobifluorene molecule is favored at the 2,2',7,7' positions[38], as it results in a more stable LUMO and a smaller HOMO-LUMO gap. This has been confirmed both through theoretical modeling and experimentally. When spirobifluorene is brominated, the primary product is the 2,2',7,7' isomer[39].

Other substitution patterns can be synthesized, however the process to do so is more difficult than simply brominating a spirobifluorene. The substituents must be added prior to the formation of the spiro center. As the spiro center is often formed via a lithiation process of dihalobiphenyls[40], the substituents must be less reactive towards organolithium reagents when compared to the aryl halides. This makes it significantly more difficult to reliably obtain, for example, 3,3',6,6' substituted spirobifluorenes.

### 1.3.1 Tetrabromospirobifluorene synthesis

2,2',7,7' tetrabromospirobifluorene is commercially available. It can also be synthesized easily via electrophilic aromatic substitution without any special conditions[39]. This tetrabrominated spirobifluorene acts as a reliable building block for a variety of compounds, as it can be easily modified through a variety of synthetic pathways, including the Suzuki coupling[41], the Sonogashira coupling[42], and the Yamamoto coupling, which we used to create our polymeric systems.

### 1.3.2 Tetrabromosilaspirobifluorene synthesis

The silicon centered analog of spirobifluorene has been described before in literature[43] and is only slightly more complicated than the spirobifluorene. The only real difference is the inability to use certain condensation reactions, such as the reaction of

2,2'-dibromobiphenyl and fluorene-9-one. The silicon center effectively requires an organolithium reagent to be used. This is usually accomplished by reacting a 2,2'-dihalobiphenyl with silicon tetrachloride[40]. Given catalysts, other methods can be used to form the spirosilabifluorene, but they are generally more expensive and use rarer materials, such as rhodium[43], when compared to an organolithium reagent. These syntheses are described in Scheme 1 and Scheme 2.

### 1.4 Silafluorene

Silafluorenes have been explored as fluorescent materials for the last few years, due to their fluorescent properties[44]. Additionally, the silicon center is predicted to have some Lewis acidity, which is potentially attractive to electron-dense molecules that show Lewis-base traits. They have very similar fluorescent properties when compared to the previously described compounds, with a high energy blue emission in the 475 nm range[45]. Silafluorene based materials have shown sensitivity towards nitroaromatic compounds via a fluorescence quenching process[45]. This is likely due to the previously mentioned Lewis acid effects of the silicon center, which would attract the relatively Lewis-basic nitro groups on the electron rich nitroaromatic molecule.

### 1.5 Nitroaromatics

Nitroaromatic compound detection is of interest for two reasons. First, nitroaromatic compounds are very toxic,[46] and used liberally in industrial settings.[47] As of 2014, 4-5 million tons of commercial nitroaromatics are produced annually.[48] Virtually all of this is nitrobenzene being produced as an intermediate to aniline, which acts as a feedstock for both polyurethane production and a large percentage of pharmaceutical production. Second, nitroaromatics are generally explosive,[49] making up some of the

most commonly used explosive compounds in history such as TNT and picric acid. Due to these factors, nitroaromatic detection has become an important topic of research in modern times. This is especially true for groundwater and soil detection, as nitroaromatic compounds do not readily degrade in environmental conditions.[50]

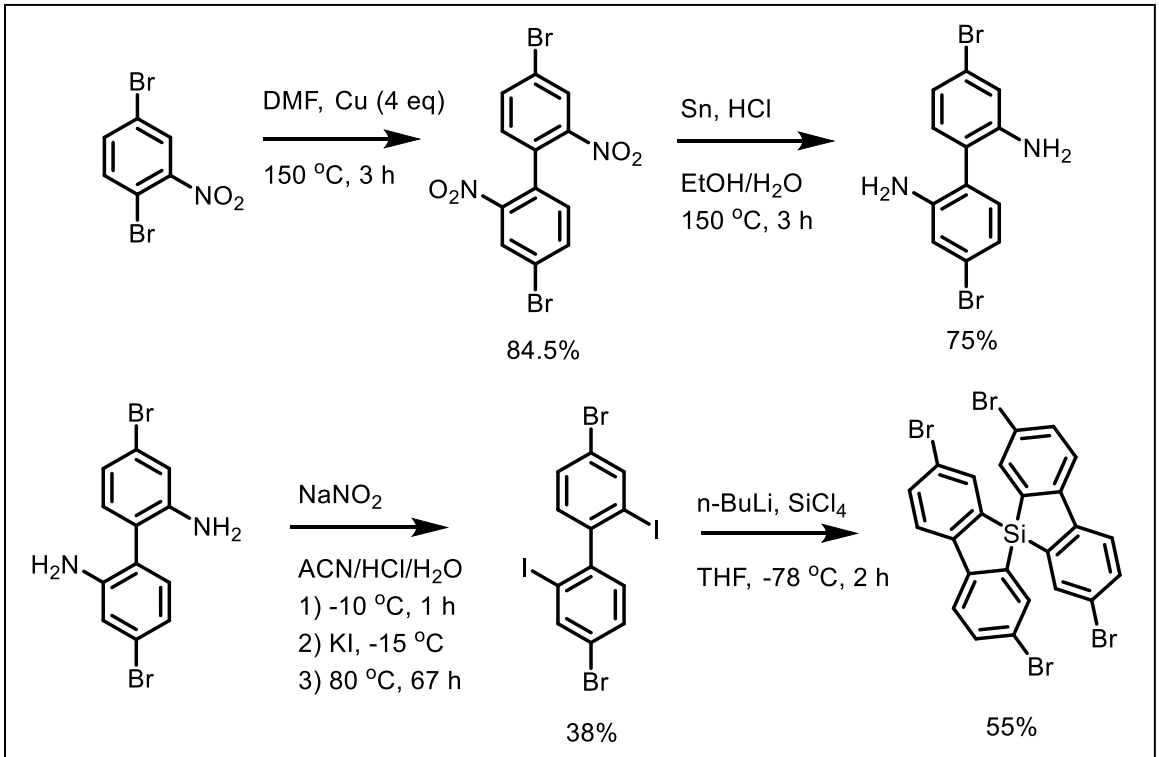


Scheme 1: Synthesis of 2,2',7,7' tetrabromosilaspirobifluorene

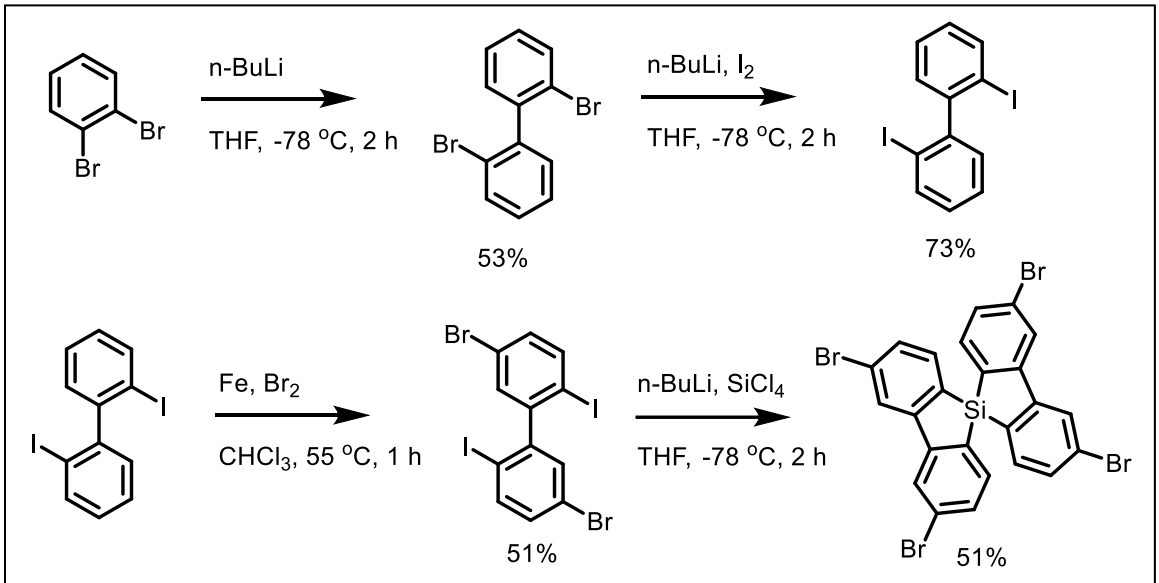


Scheme 2: Synthesis of 3,3',6,6'-tetrabromosilaspirobifluorene

## 1.6 Fluorescence Quenching

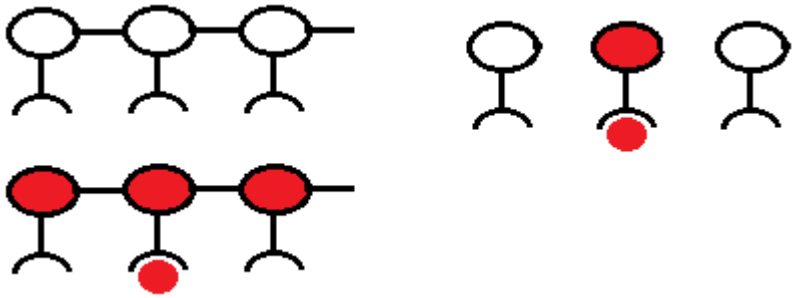

Figure 7: (left) Quenching distributed by molecular wire effect, (right) localized quenching only

The primary reason for the high sensitivity of the polymeric system lies in the conjugation present throughout the polymer. This allows the polymeric system to amplify the molecular recognition signal via electron migration along the polymer backbone. This is an improvement over a small molecule sensor, as the required analyte concentration for complete quenching is no longer equivalent to the concentration of the small molecule sensor. As any individual part of the polymer gets quenched, the rest of the polymeric network is also quenched due to the "molecular wire" effect (Figure 7). This is caused by the transport of excitons down the electronically conductive polymer backbone. The relative ease of transporting excitons down the molecular wire allows light energy absorbed by a fluorophore to "migrate" to a quenching site, where it can undergo a series of non-radiative transitions to relax back to a ground state without a fluorescent effect. This effect is limited by distance and the ability of the polymer to conduct excitons.

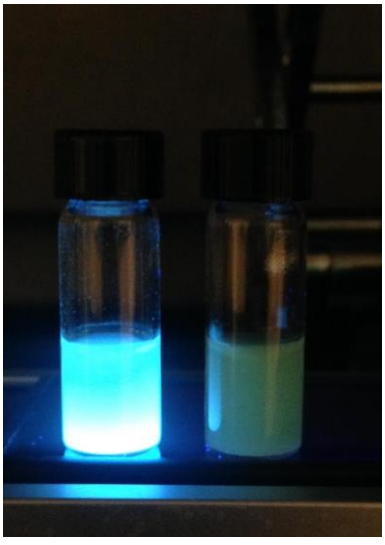

Figure 8: (left) a fluorescent suspension, (right) a quenched fluorescent suspension

A basic principle of fluorescence, and the one that makes fluorescence emission detection both possible and an attractive method for sensor design, is the concept of the Stokes shift. This phenomenon, first observed by Sir G. G. Stokes in 1852, is caused by a rapid decay of absorbed energy to the lowest vibrational level of the first excited singlet state, $S_1$. The minor conversion of some of the excitation energy to vibrational thermal energy before emission results in an emission that is lower in energy and has a longer wavelength. This allows simple detection of the emission by excluding the excitation wavelength from the detector to avoid background interference from the excitation source. Another important property of fluorescence comes from the rapid relaxation to the $S_1$ state observed in fluorophores. As a result of this rapid (generally on the order of $10^{-12}$ seconds) relaxation, the emissions wavelength will always be consistent for the same fluorophore regardless of the excitation energy. This is known as Kasha's rule. Upon excitation into higher electronic and vibrational levels, the excess energy is quickly dissipated until the fluorophore is left in the lowest vibrational state of the $S_1$ electronic state. Recent advances have shown some exceptions. This is generally caused by fluorophores that exist in multiple ionization states, each of which has its own excitation and emission wavelength. Some molecules have shown emissions from the $S_2$ state; however, this is very rare.

Two important characteristics for a fluorophore are the fluorescence lifetime and quantum yield. Quantum yield refers to the ratio of emitted photons relative to absorbed photons. The largest quantum yield fluorophores, such as noble metal complexes, approach unity and display the brightest emissions. Lifetime is important as it defines the time available for the fluorophore to interact with its environment, which is particularly

important for certain types of fluorescence quenching that involve collisions between separate molecules. As fluorescence emission is a random process, the fluorescence lifetime is a statistical measure, defining the average time that a fluorophore spends in the excited state. This is described in equation 1 (Eq 1) where $\tau_n$ is the excited state lifetime, $\tau$ is the measured lifetime, and Q is the quantum yield.

Eq 1: $\tau_n = \tau/Q$

Fluorescence quenching refers to the many mechanisms by which the phenomenon of fluorescence emission can be decreased. The simplest of these mechanisms is dynamic quenching, which occurs when a collision between a fluorophore and a quencher allows a non-radiative transition to occur from the excited state to the ground state, bypassing the emission of a photon. This occurs without any permanent chemical change in the components. Such quenching is described by the linear Stern Volmer relationship shown in equation 1 (Eq 2), where the constant $K_{SV}$ is the product of the bimolecular quenching constant $k_q$ and the unquenched emission lifetime $\tau_0$. This is due to the collision requirement, where the molecular interaction must occur in the window between excitation of the fluorophore and emission of a photon. The constant $K_{SV}$, in this case, indicates the sensitivity of the fluorophore to being quenched.

Eq 2: $\frac{I_0}{I} = 1 + K_{SV}[Q] = 1 + k_q\tau_0[Q]$

Another common type of quenching is static quenching, which is described by a similar equation (Eq 3). The key difference between dynamic and static quenching lies in the interaction between the fluorophore and the quencher. Where dynamic quenching relies on a collision between the excited fluorophore and the quencher, static quenching occurs due to the formation of a metastable complex between the fluorophore and the

quencher in the ground state, prior to excitation of the fluorophore. As a result of this complex formation, the $\tau_0$ term is dropped, as the lifetime of the emission does not matter. Due to the complex formation, there is no time window in which a collision must occur, and so the proportionality constant $k_q$ corresponds to the bimolecular association constant for the formation of the fluorophore-quencher complex. Fluorescence lifetime can be used to distinguish between static and dynamic quenching mechanisms. In dynamic quenching, fluorescence lifetime of the excited state fluorophore will be shortened in the presence of quencher, and $\tau_0/\tau$ will be equal to $I_0/I$. On the other hand, when the main mechanism of quenching is caused by static association, there is no variation in emission lifetime based on concentration of quencher, and therefore the ratio of $\tau_0/\tau$ equals one.

Eq 3: : $\frac{I_0}{I} = 1 + k_q[Q]$

1.7 Current Technology

Current nitroaromatic sensors operate on several different principles, depending on their applications. Most of these detectors fall into some sort of colorimetric category, with fluorescence-based sensor technology being a recent focus.[51] Other standard detection methods involve mass spectrometry,[52] a method that is entirely infeasible for rapid field identification, as well as dogs specifically trained to detect explosives,[53] which require additional considerations to maintain viability, such as food and proper training.

Current research focuses on the development of a chemical "nose".[54] This involves creating an array of chemical sensors that is capable of both detecting and distinguishing compounds based on their chemical properties. Such a nose would be able to not only detect the presence on nitroaromatic compounds in the sample, but also

identify the exact compounds that show up in the sample. This requires an array of sensors that operate in tandem, ideally giving a distinct result based on the compounds analyzed. This can be achieved by either using multiple distinct sensors, such as having a single testing strip with a dozen different testing sites, or by having sensors that give off distinct data, such as having sensors that provide analyte specific color responses.

In both cases, the structure of the sensor itself is important. For chemical sensors that interact with their environments, porosity and surface area are extremely important variables. Many different approaches have been considered to maximize these properties. Previously, spiro-centered polymer compounds have been discussed. However, other similarly effective methods, such as iptycenes,[55] have been discussed in the literature.

1.8 Goal of Research

The primary goal of this research is to synthesize and characterize two novel spirosilabifluorene networks, the 2,7-polyspirosilabifluorene and the 3,6-polyspirosilabifluorene polymers shown in Figure. We will also prepare a known 2,7-polyspirobifluorene network to compare the chemical properties. We believe that the silicon central atom will impart favorable electronic properties to our polymeric network, allowing it to be a more effective substrate for a nitroaromatic sensor.

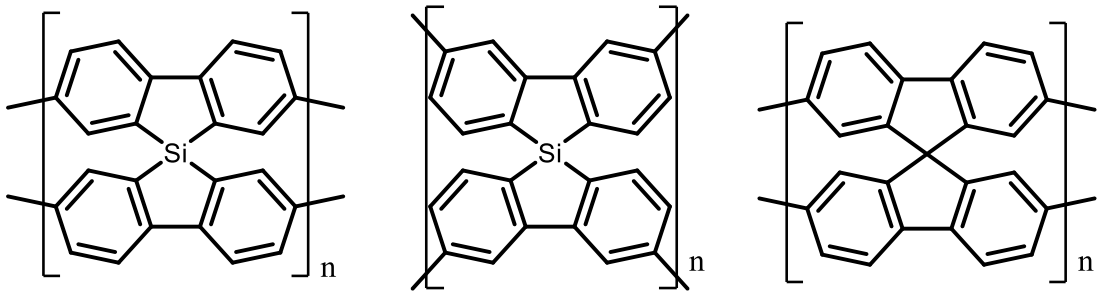


Figure 9: (left to right) 2,2’,7,7’-polyspirosilabifluorene; 3,3’,6,6’-polyspirosilabifluorene; 2,2’,7,7’-polyspirobifluorene

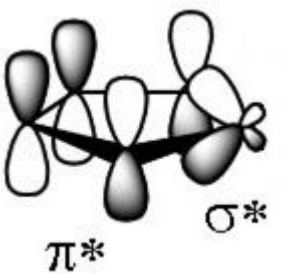


Figure 10: The LUMO orbital of a silacyclopentadiene ring displays the π*-σ* orbital overlap[1]

As the sila-analog of spirobifluorene, we expect there to be similar properties between the known spirobifluorene network and the silaspirobifluorene networks. Condensed homopolymeric networks consisting of spirobifluorene have been synthesized and isolated in the past, showing unique fluorescence properties previously described.[56] The substitution of the silicon atom for the carbon atom provides us with favorable electronic conjugation with the surrounding aromatic system when compared to carbon. This is caused by the silicon atom donating electrons from the low-lying $\sigma^*$ orbital to the π* orbital of the butadiene.[57] We also believe, based on modeling, that the silicon atom will act as a Lewis acid. The Lewis acidity of the silicon atom would allow it to attract the relatively basic, electron rich, nitro group of a nitroaromatic compound. The modeling results, shown in Figure 11, seem to confirm this conclusion.

The four possible polymer morphologies were combined with a trinitrobenzene molecule, and the energy of their interaction was calculated. The polymer networks conjugated at the 2 and the 7 positions are consistently lower in energy than those of the top row. Further, the silicon centered spirosilabifluorene networks form consistently more stable complexes with trinitrobenzene when compared to the spirobifluorene networks. Based on these modeling results, we hypothesized that the silicon centered spirosilabifluorene network conjugated at the 2 and the 7 positions would give us a much

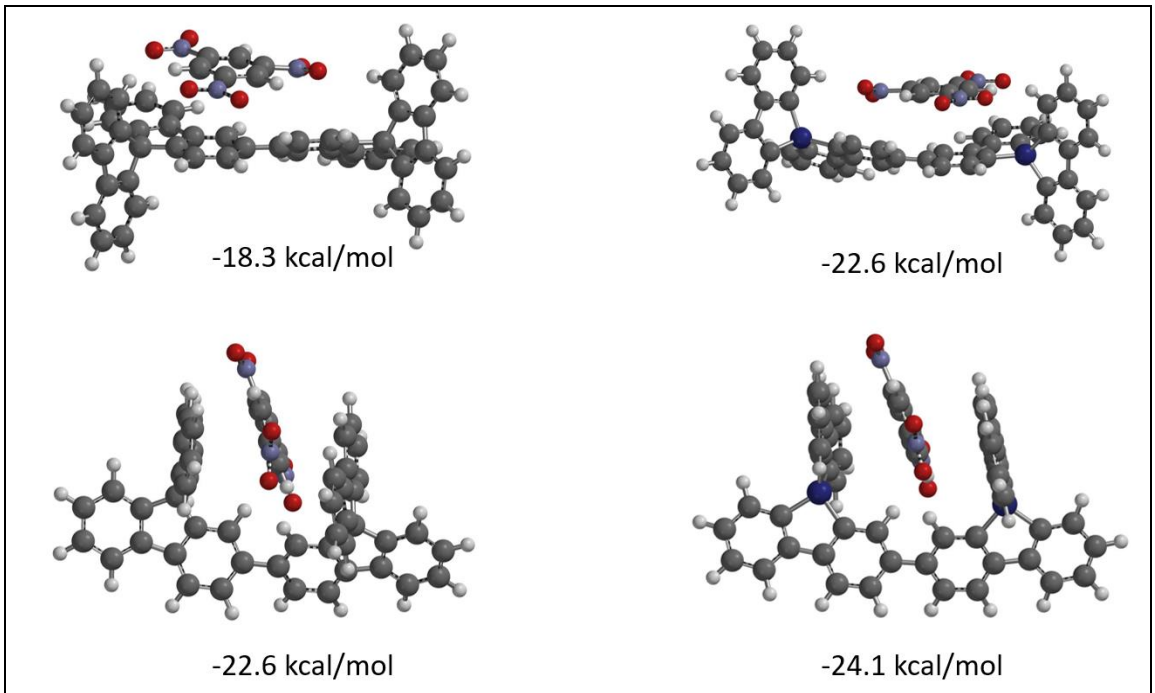


Figure 11: Complex energy calculations for (clockwise from top left) 3,6 conjugated spirobifluorene, 3, 6 conjugated spirosilabifluorene, 2, 7 conjugated spirosilabifluorene, 2, 7 conjugated spirobifluorene with 1,3,5-trinitrobenzene

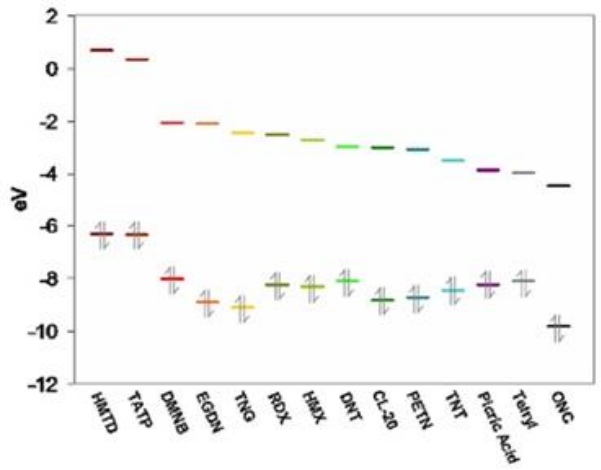


Figure 12: LUMO and HOMO levels of various explosive compounds. [1]

higher association constant for the complex, therefore generating a steeper slope on the Stern-Volmer quenching plot. This would allow us to create a more sensitive sensor for nitroaromatic compounds, capable of detecting toxic and potentially explosive materials. Further, exploitation of the optoelectronic properties of the spirosilabifluorene network, and the inherent tunability of the band gap via addition of other aromatic spacers, provides the possibility of selective detection of nitroaromatic compounds based on their individual bandgaps. As non-radiative fluorescence quenching requires an electron transfer from a higher energy fluorophore SOMO to a lower energy quencher LUMO, a variety of sensors can be created simply by altering the SOMO energy level of the polymeric network. Tuning the SOMO to optimize the fluorophore SOMO-quencher LUMO energy overlap would allow lowering the energy barrier for electron transfer. Such processes would also alter the bandgap of the polymer network. As demonstrated by Lee et. al.[58], the polyspirosilabifluorene has a redshifted emission spectrum in the visible range when compared to the carbon centered analog, therefore alterations to the SOMO energy level would likely result in fluorescent that is in the normal visual range. This would not only improve the detection of possibly dangerous materials; it would also allow rapid field identification of the nitroaromatic in question on a visual basis without any specialized equipment. The various LUMO levels

of nitroaromatic compounds are described in Figure 12. The structures of the nitroaromatics described are shown in Figure 13.

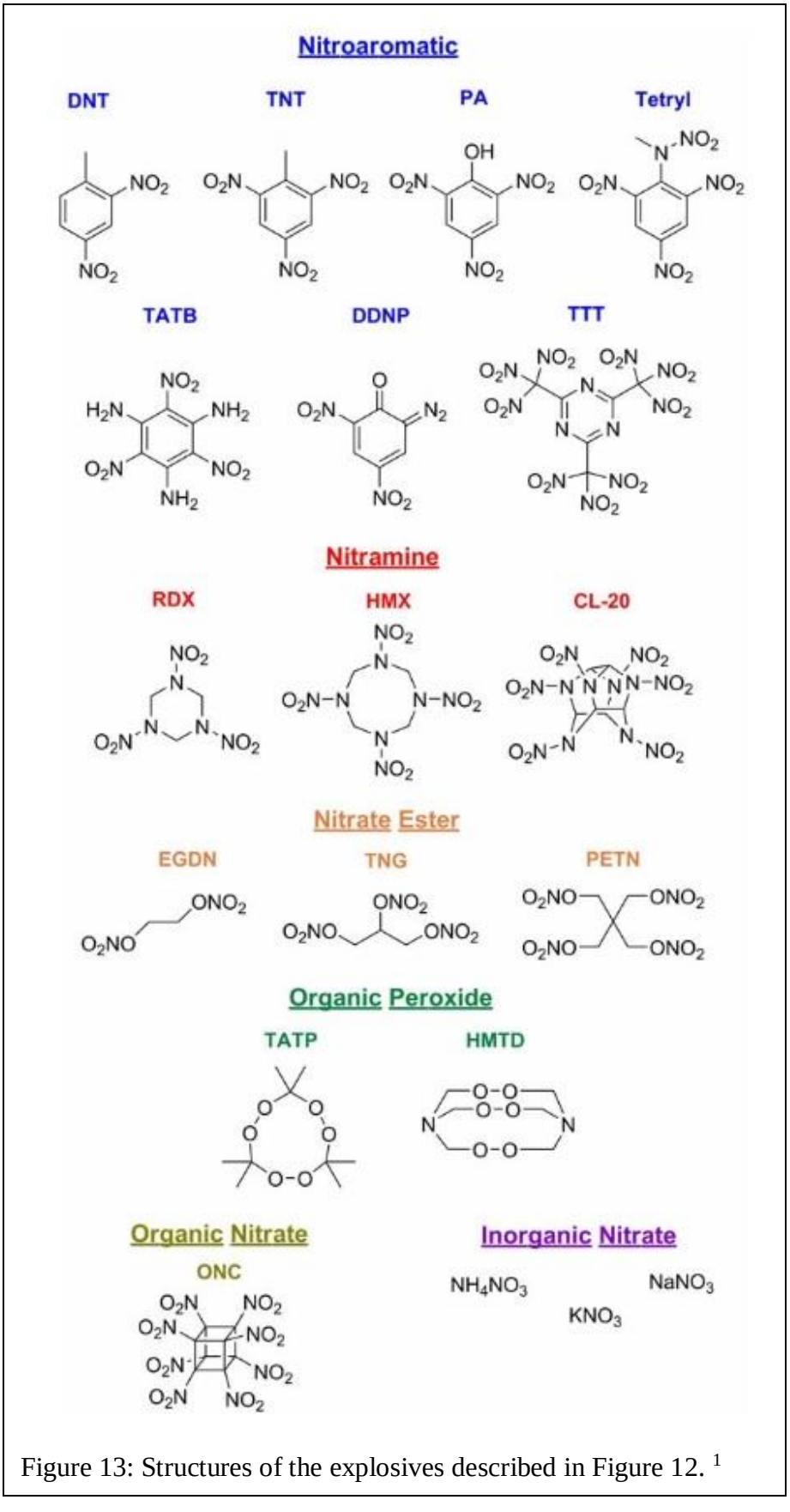


Figure 13: Structures of the explosives described in Figure 12. [1]

As we can see, the LUMO levels for most common explosives are similar, but still vary by up to 2 eV. If we can tune the polymeric framework to generate specific SOMO energies just above the LUMO levels of the analyte in question, we can create a series of distinct polymeric systems that would show different fluorescence quenching based on the identity and electrochemical properties of the analyte.

# CHAPTER 2: RESULTS AND DISCUSSION

## 2.1: Synthesis and characterization of porous spirosilabifluorene networks

2,2',7,7'tetrabromospirobifluorene, was polymerized according to previously published procedure[59]. The same method was used to polymerize 3,3',6,6' spirosilabifluorene, and 2,2',7,7' spirosilabifluorene. This procedure is described in detail in Scheme 3 and Scheme 4.

### 2.1.1 Synthesis of porous networks

The synthesis of the polymeric spirobifluorene and spirosilabifluorene network system was carried out successfully from a tetrabromospirobifluorene and tetrabromospirosilabifluorene system. This was done successfully in air-free conditions using a Yamamoto coupling procedure, using the tetrabromo compounds. This procedure was reliably carried out to result in a polymeric system for all three starting materials, the 2,2',7,7' tetrabromospirobifluorene, the 2,2',7,7' tetrabromosilaspirobifluorene, and the 3,3',6,6' tetrabromospirosilabifluorene monomers. The Suzuki coupling led to a brilliant purple reaction mixture, shown in Figure 2, which was indicative of the successful procedure. As the polymerization was carried out with

Figure 14: Purple polymerization of tetrabromospirosilabifluorene

nickel cyclooctadiene, any air would have turned the reaction mixture black, creating an obvious indication that the reaction had failed.

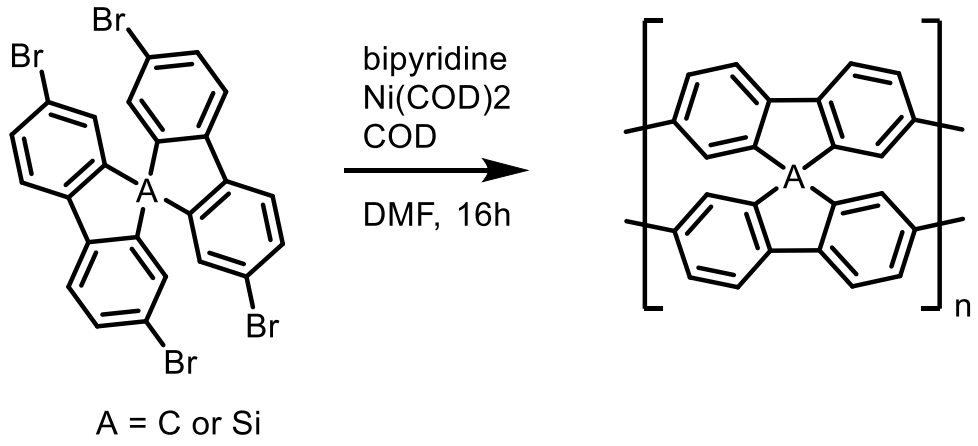


Scheme 3: Synthesis of 2,7-polymer system

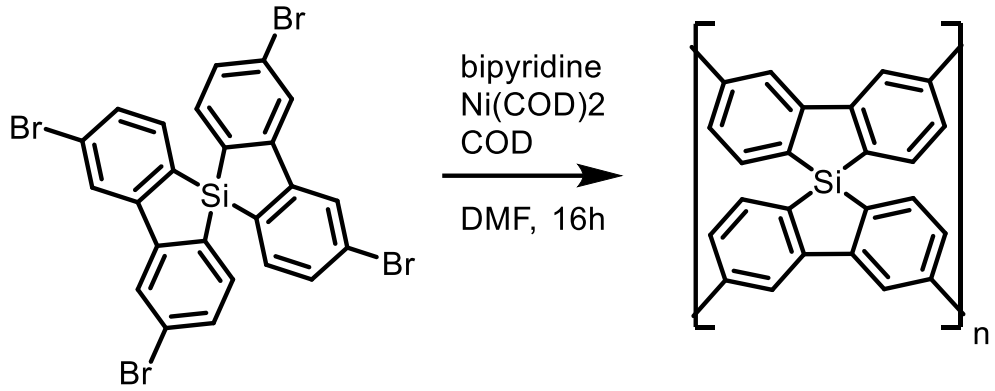


Scheme 4: Synthesis of 3,6-polyspirosilabilfuorene system

2.1.2 Material Characterization

Confirmation was carried out by elemental analysis. Combustion analysis significantly underestimated the carbon content of the polymer network, likely due to the extreme thermal stability of the polymeric networks as well as the formation of silicon carbide, an extremely stable ceramic material. However, this is consistent with previously obtained combustion analyses in literature[59]. Elemental analysis via Energy Dispersive

X-ray Analysis (EDAX) gave values that were much closer to the expected mass percentages. There is no evidence of leftover bromine. This is described in Figure 15.

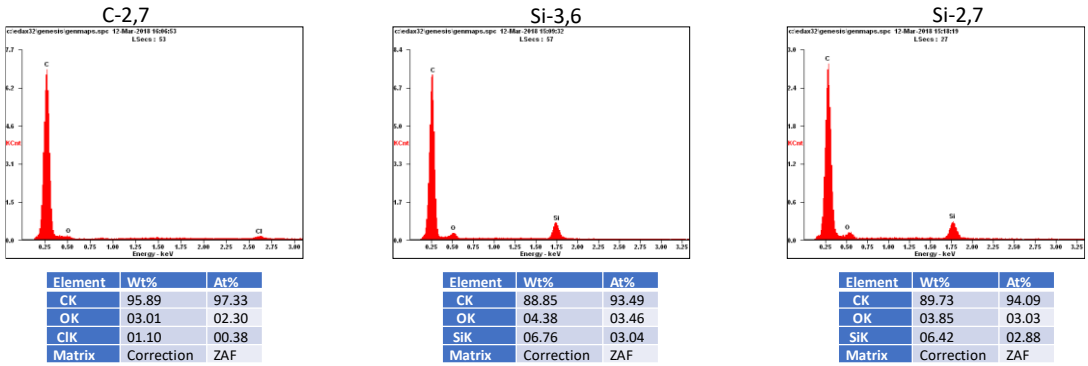


Figure 15: EDAX results for the three polymeric compounds.

Table 1, below, shows the expected mass percentages for all three polymeric compounds. When compared to the results in Figure 14, it is apparent that the mass percentages line up as expected. The combustions analysis (labeled as experimental) is consistently short of the true carbon percentage value, which is reflected in the literature for the known carbon-centered compound. While the carbon compound has no way of forming a silicon carbide biproduct, the deviation from expectation for the silicon centered compounds are

Table 1: Expected and experimental mass percentages for all three polymeric compounds by combustion analysis

| | C | H | N | Si |
|---|---|---|---|---|
| Theoretical C-2,7 | 96.1 | 3.9 | 0 | |
| Exp. C-2,7 | 93.1 | 4.5 | 0.4 | |
| literature | 89.3 | 4.2 | 0.2 | |
| Theoretical Si-3,6 | 87.8 | 3.7 | 0 | 8.6 |
| Exp. Si-3,6 | 81.8 | 4.4 | 0.4 | ND |
| Theoretical Si-2,7 | 87.8 | 3.7 | 0 | 8.6 |
| Exp. Si-2,7 | 80.9 | 4.4 | 0 | ND |

consistent with carbide formation. The mass inconsistency within the carbon centered compound is likely due to pyrolytic graphite formation due to incomplete combustion within the polymer framework.

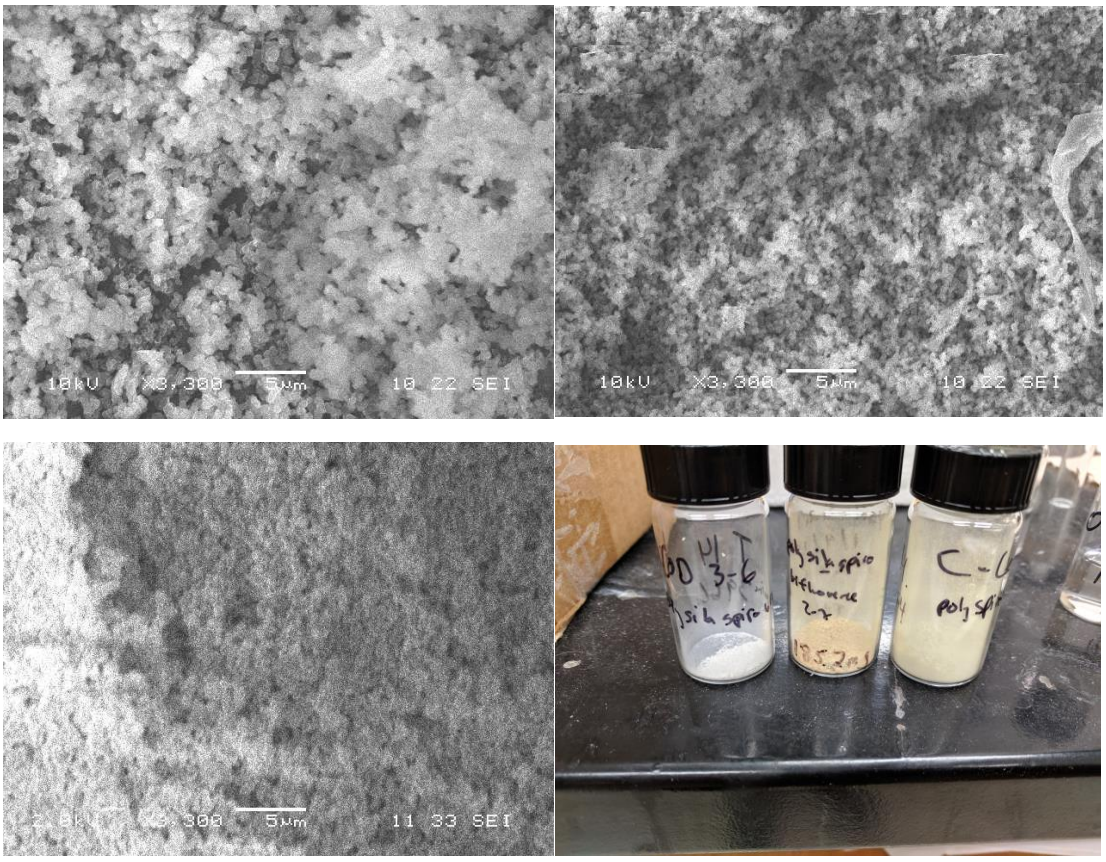


Figure 16: SEM images of (top left) 2,7 polyspirobifluorene, (top right) 3,6 polyspirosilabifluorene, (bottom left) 2,7 polyspirosilabifluorene, and (bottom right) all three compounds, in order from left to right: 3,6 polyspirosilabifluorene, 2,7 polyspirosilabifluorene, and 2,7 polyspirobifluorene

SEM images were also taken of all three compounds, resulting in Figures 16. The SEM images we obtained appear to show a high surface area porous material. Further, the SEM seems to indicate aggregates of submicron sized particles, with little discernible difference between the three structures.

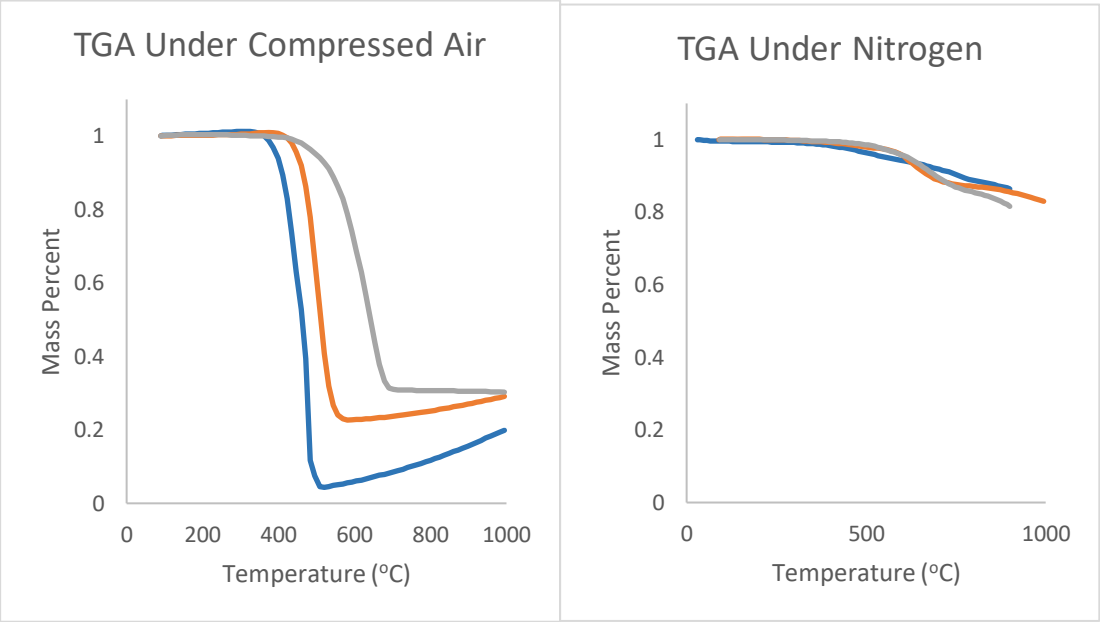


Figure 17: Thermogravimetric analysis of the polymers under compressed air and under nitrogen. The blue trace is the carbon centered polymer, the orange trace is the si-2,7 polymer, and the gray trace is the si-3,6 polymer.

Thermogravimetric Analysis (TGA) measurements were carried out. They were consistent with previous literature[59], for the 2,7 carbon centered system, with very similar results for the novel silicon centered polymers. Mass loss was first observed near 400°C under atmospheric conditions and approximately 600°C under nitrogen. This is significant for two reasons. First, it means that the polymer is quite stable and will not easily degrade. This makes the polymer more attractive from a conservation standpoint, as it will likely be reusable. Second, the adsorbed analyte could potentially be boiled off by heating the polymer, simplifying the cleaning process for reuse. As the nitroaromatic compounds for which the sensor is active all boil at relatively low temperatures in the 200°C range, this is a viable method for regenerating the sensor.

Further, the polymer shows insignificant mass loss under a nitrogen atmosphere, even if heated to 1000°C, the limit of our instrument. However, the lack of mass loss

does not necessarily mean that the polymer is not degrading. It is entirely likely that while very little chemical degradation occurs, there are significant structural changes happening to the polymer. Due to the spiro-aromatic structure, there should be very little loss in porosity within the structure without chemical degradation. This is one of the strengths of PIM systems, as porosity cannot be easily destroyed by rearrangement of the polymer, and necessarily requires destruction of the monomer structure. This effectively removes concerns about glass transition temperature, which affect most inorganic porous materials, as well as organic materials capable of rearranging into crystalline structures with π-π interactions.

Another possibility that we have considered is that the polymer is degrading into stable ceramics, such as silicon carbide. This was due to the results of our combustion analysis, carried out by Atlantic Microlabs. The results consistently showed lower carbon percentages than expected. This is also consistent with literature analysis of the known carbon compound[59]. This is likely due to incomplete combustion of the extraordinarily stable polymer giving false weight readings. This could be tested by attempting to do a BET analysis on combusted samples to see if they maintain their porosity and surface area. If the sample remains somewhat porous with a higher surface area, then degradation is not occurring. If the sample loses porosity or surface area, then it is likely degrading into stable, but unwanted, compounds. This idea was confirmed by EDAX measurements, which gave results much more in line with the expected atom and mass percentages. This is described in Figure 14.

2.1.3 Surface area measurements

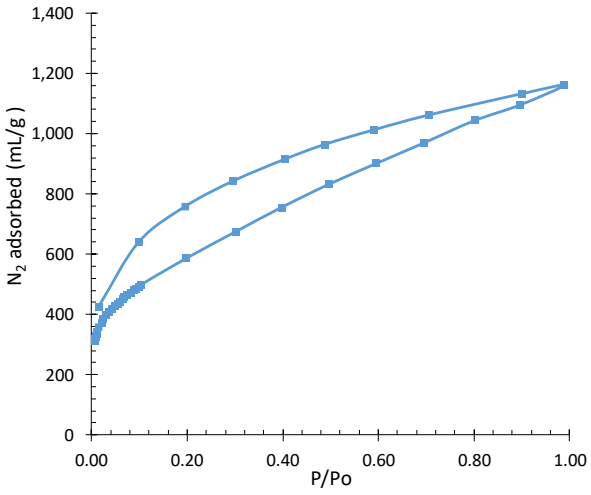


Figure 18: Isotherm of $N_2$ gas adsorbed onto the 2,7-polyspirobifluorene polymeric system.

Surface area for the three materials were determined using a BET surface area analyzer. Nitrogen was used as the adsorbent. An isotherm indicating significant adsorbtion at low pressures and with significant hysteresis was obtained (Figure 18). This isotherm is indicative of a microporous material.

Surface area is calculated from the adsorption isotherm using Brunauer-Emmett-Teller (BET) theory according to Equation 4.

Eq 4: $$\frac{{}^{p}/_{p_0}}{n\left(1-{}^{p}/_{p_0}\right)} = \frac{1}{n_m C} + \frac{C-1}{n_m C}\left({}^{p}/_{p_0}\right)$$

In this equation, $n$ is the specific amount of gas adsorbed at relative pressure ${}^{p}/_{p_0}$, and $n_m$ is the specific monolayer capacity. $C$ refers to the energy of the monolayer adsorption. The higher the value of $C$, the more interaction. For a BET measurement that is used to calculate an apparent surface area, The $C$ constant generally needs be positive[60].

The BET plot is only linear in a certain range, as the layer of adsorbed molecules ceases to be a monolayer and begins to fill in an uneven multilayer fashion. As a result, there are several constraints for determining the appropriate data range to be used in BET surface area caluclations for a microporous material. First, the quantity $C$ must be positive. Second, the application of the BET equation must be limited to the range where $n(1 - {}^{p}/_{p_0})$ continuously increases with $({}^{p}/_{p_0})$. Finally, the $({}^{p}/_{p_0})$ value corresponding to $n_m$ should be within the selected BET range, as if $({}^{p}/_{p_0})$ increases past $n_m$, this is evidence of multilayer formation. The second constraint can be tested by plotting $n(1 - {}^{p}/_{p_0})$ versus $({}^{p}/_{p_0})$, as shown in Figure 19. We pick the local maxima, and then plot those values onto a BET plot, shown in Figure 20. Using this plot,

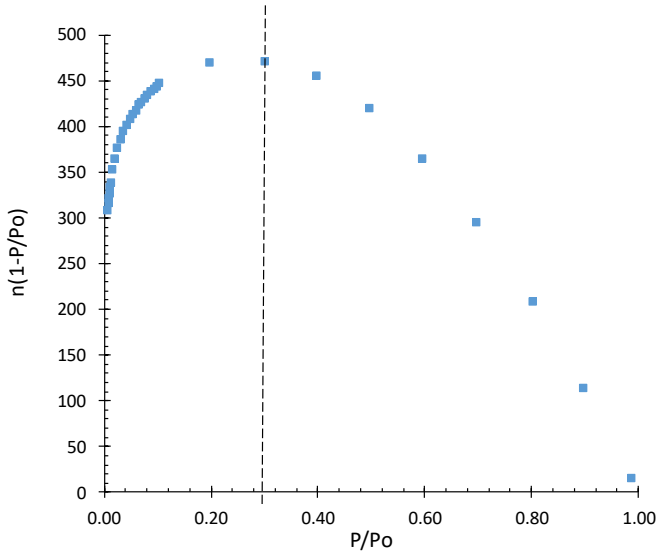


Figure 19: Maximum value of $n(1 - {}^{p}/_{p_0})$ to fulfill continuous increase requirement

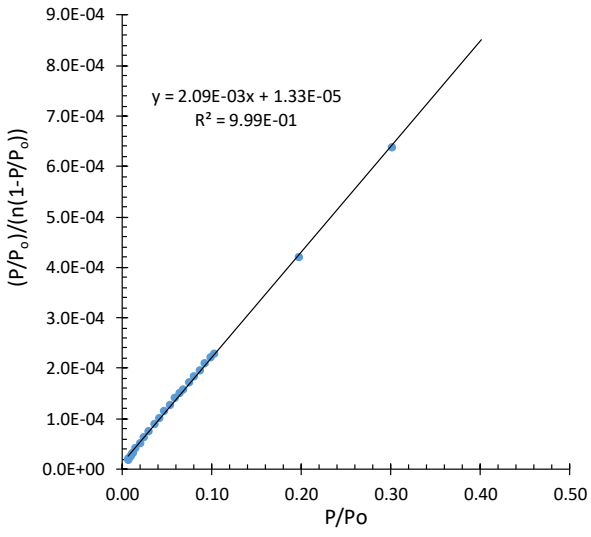


Figure 20: BET transform plot

we can calculate the value of $C$ by dividing the slope by the intercept plus one, based on the constants shown in equation 4. Using this calculated $C$ value, we can calculate the $n_m$ value by dividing the $C$ value by the intercept of the graph. However, when we do this, we realize that our graph no longer fulfills the final condition required for BET theory, as the $\left({}^{p}/_{p_0}\right)$ value rises past $n_m$, evidence of multilayer formation. As a result, we must adjust our choice of data slightly, as shown in Figure 20.

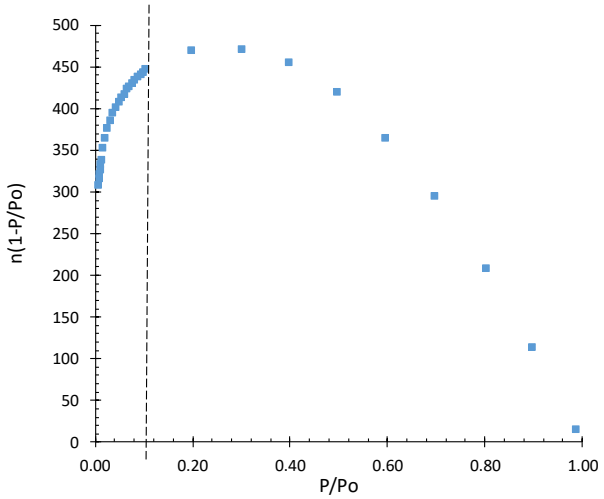


Figure 21: Adjusted $n\left(1-{}^{p}/_{p_0}\right)$ versus $\left({}^{p}/_{p_0}\right)$ plot to comply with condition 3.

This gives us a modified BET transform plot, as we discard the furthest two data points. This adjusted BET transform plot is shown in Figure 22.

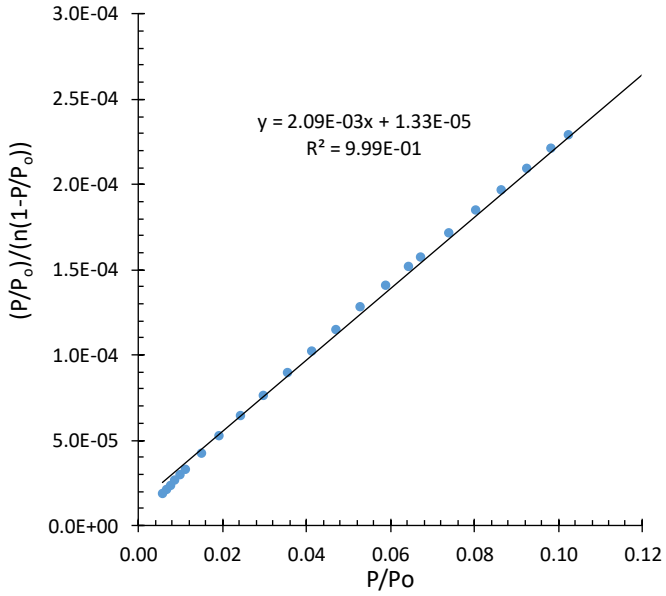


Figure 22: Adjusted BET transform plot to comply with condition 3.

Now that our adjusted BET transform plot complies with all three conditions for microporous analysis, we can use the data to calculate the surface area of our polymer network. This is done based on several factors. First, we know based on our previous calculations that we have a monolayer of our adsorbing gas on the surface of the polymer. Second, we know the cross-sectional area of our adsorbing gas (nitrogen) from previous literature values[61]. Finally, we know the monolayer capacity of our polymer. This allows us to use equation 5 to calculate a specific BET area $a_s(BET)$.

Eq 5: $a_s(BET) = n_m * L * \frac{\sigma_m}{m}$

In this equation, $\sigma_m$ is the cross-sectional area of the adsorbing gas, and $m$ is the mass of the gas. The $L$ constant is a conversion factor that converts from volume of adsorbate to number of adsorbate molecules (Avogadro's number/molar volume, 22.4 L/mol).

Given the above numbers and equation, we can calculate our surface area per gram of polymer system. The graphs in Figures 17-21 are the data for the 2,7-polyspirobifluorene system, as this system is previously known in literature[59] and can be

used as a useful test of our calculations. The results from these calculations are shown in Table 2.

Table 2: A summary of the values generated through BET analysis of our polymeric systems, complete with calculated surface area in square meters per gram. The top row shows the literature value for the 2,7-C system as comparison.

| | slope | intercept | C | $n_m$ | SA (m^2/g) |
|---|---|---|---|---|---|
| 2,7-C (lit.) | | | | | 1970 |
| 2,7-C | 0.00219 | 0.00000962 | 228 | 454 | 1980 |
| 2,7-Si | 0.00306 | 0.0000114 | 269 | 325 | 1420 |
| 3,6-Si | 0.00286 | 0.0000039 | 734 | 349 | 1520 |

A DFT calculation was carried out as well to calculate the pore size of the polymer compounds. The mode of the pore sizes was 1.686 nm for the 2,7 conjugated systems, and 1.487 nm for the 3,6 conjugated system. Spartan calculations were carried out on a TNT molecule, which gave us a maximum length of 6.442 angstroms. This means that TNT, as well as the other similarly sized analytes should easily pass into the porous polymer structure, allowing effective fluorescence quenching.

2.1.4 Optical Properties

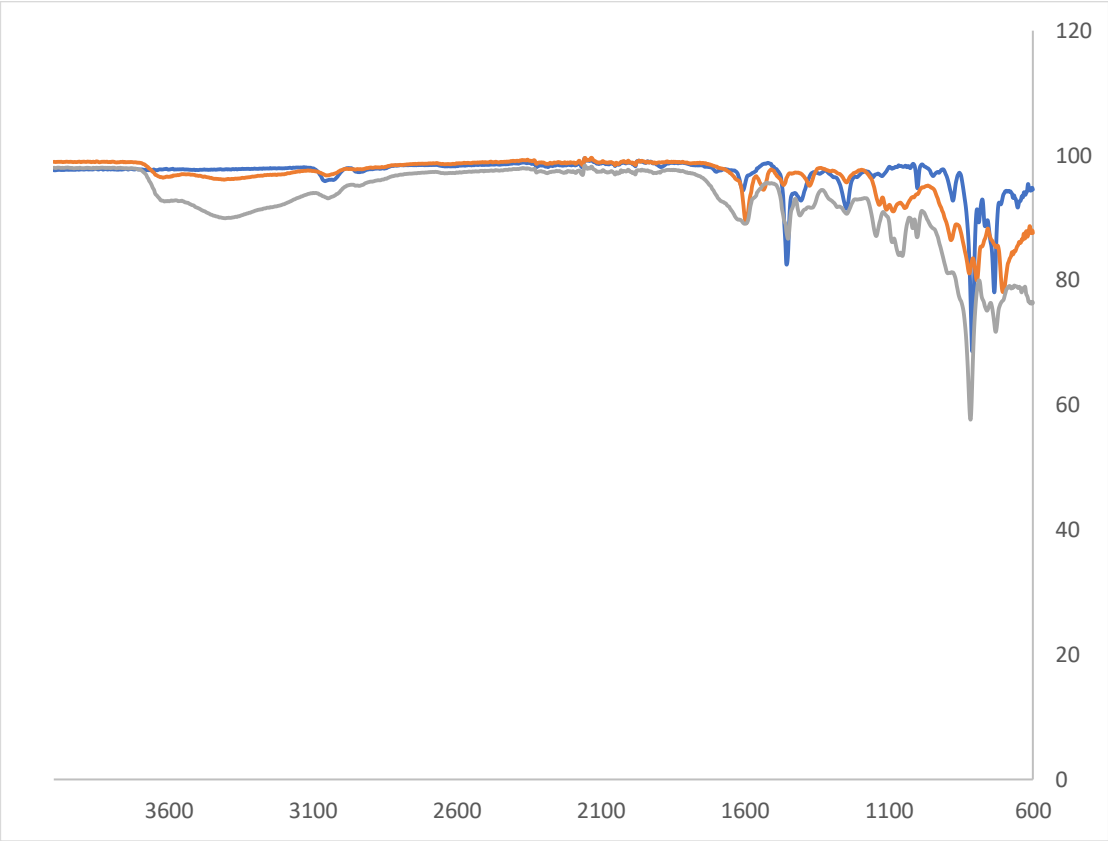


Figure 23: ATIR spectra of all three compounds. The blue trace is 2,7-polyspirobifluorene, the orange trace is 3,6-polyspirosilabifluorene, and the gray trace is 2,7-polyspirosilabifluorene

The IR gives very little information. There is a clear sp2 carbon peak for all three compounds around 3000 $cm^{-1}$, backed by a similar aromatic sp2 carbon peak in the fingerprint region, near 1650 $cm^{-1}$. The silicon center does not appear to modify the IR spectra to any significant degree.

The excitation and emission spectra, on the other hand, are much more interesting. Both of the 2,7 compounds have high energy blue emissions at approximately 450nm, while the 3,6 compound has an emission wavelength at approximately 400nm.

As before, this clearly shows that the difference in the HOMO of the two compounds is significant.

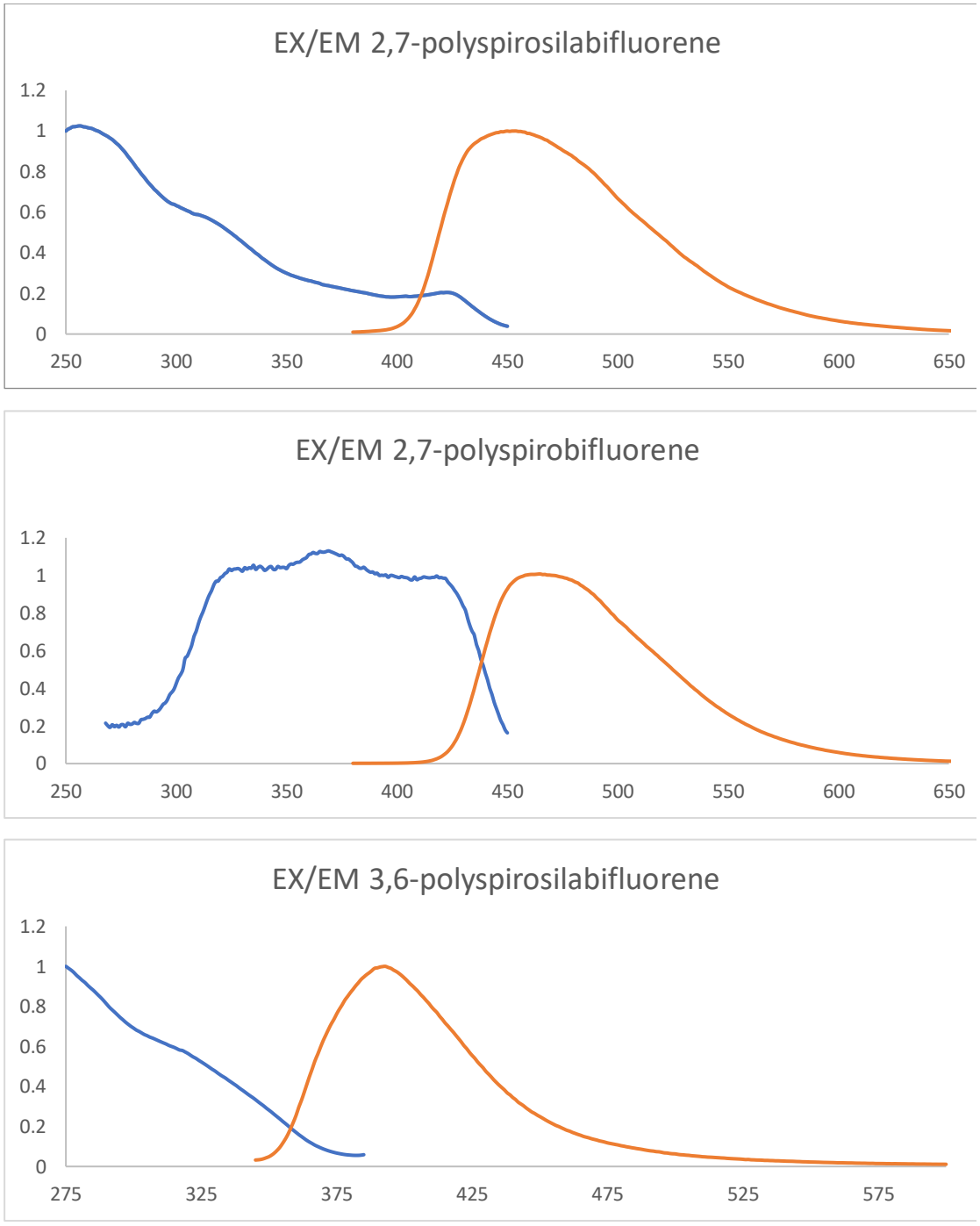


Figure 24: Excitation (blue) and emission (orange) traces for the (top to bottom) 2,7-polyspirosilabifluorene, 2,7-polyspirobifluorene, and 3,6-polyspirosilabifluorene. Note that the x axis is shifted for the 3,6 system.

As a final test of our model validity, we compared the bandgap energy differences between various polymer lengths and conjugation positions of the polymer system. The results are described in Figure 25. As the graphs of the LUMO and the HOMO energy levels show, the relevant pentamer is a good approximation for the polymeric system, with the HOMO-LUMO gap stable when compared to the shorter polymer chains. The

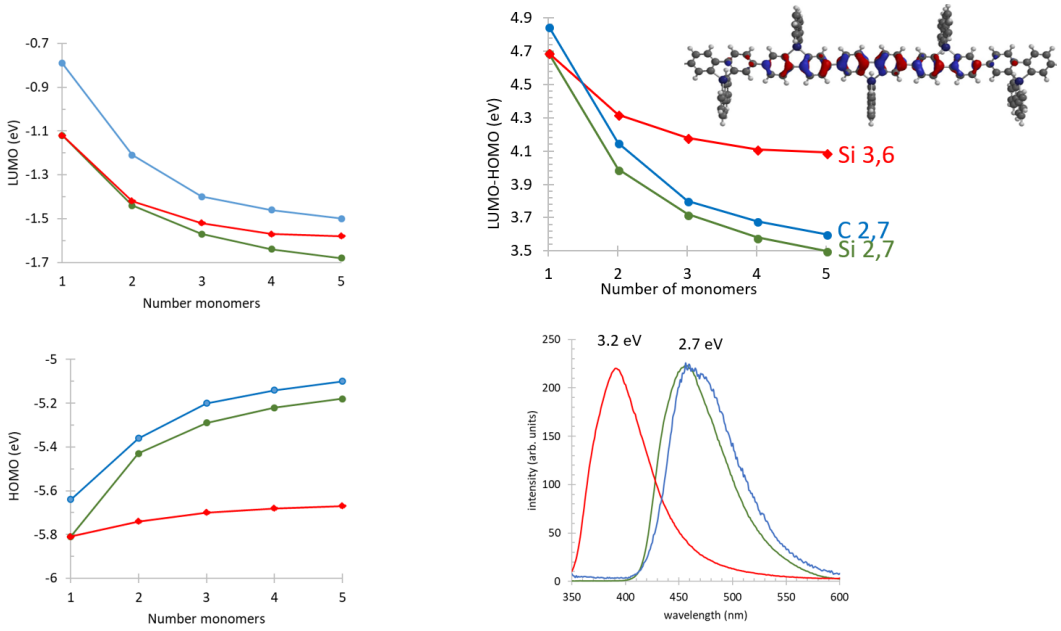


Figure 25: Graphs of the (clockwise from top right) LUMO, HOMO compared to polymer chain length, Experimental emissions wavelength, and calculated bandgaps (HOMO-LUMO)

bottom left chart shows that the emission wavelength of the polymeric network has a bandgap which is very close to that predicted by modeling the bandgap of the polymeric system. This simultaneously supports the validity of the electronic modeling previously done for this system, as well as confirms the increased stability of the 2,7-conjugated polymeric system when compared to the 3,6-conjugated system.

2.1.5 Stern-Volmer Quenching Studies

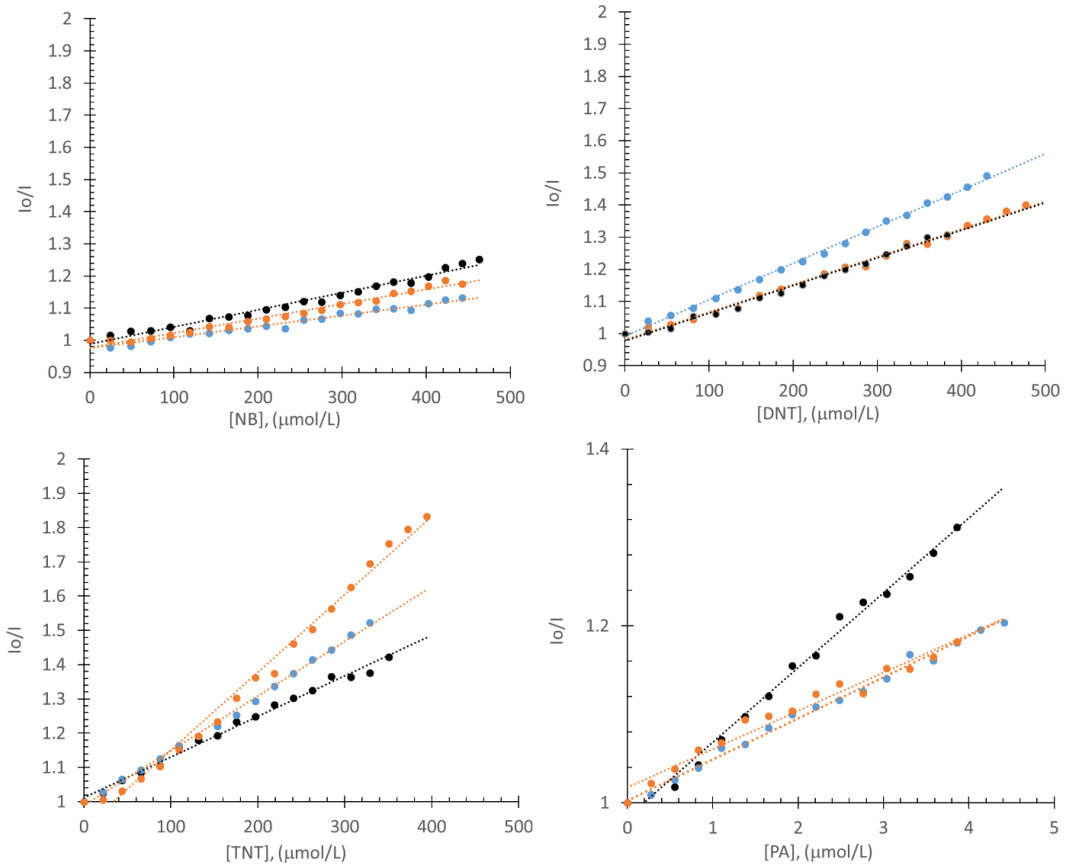


Figure 26: Stern-Volmer plots of conjugated polymer systems quenched by (clockwise from top left) nitrobenzene, dinitrotoluene, picric acid, and trinitrotoluene. Blue trace is 3,6 polyspirosilabifluorene (3,6-Si), orange trace is 2,7 polyspirobifluorene (2,7-C), and the black trace is 2,7 polyspirosilabifluorene (2,7-Si).

Preliminary quenching experiments using picric acid as the quencher were carried out to test the fluorescence quenching of the polymeric system. The initial results, shown in Figure 8, show that the polymeric system is sufficiently quenched by the picric acid, and more detailed results, shown in Figure 24, display a reasonable quenching curve. This shows the validity of the polymeric system as a platform for a nitroaromatic sensor. This was achieved by measuring the fluorescence quenching effect through fluorescence spectrometry, by plotting the quenching of polymer fluorescence versus concentration of

the nitroaromatic analyte. Fluorescence quenching is very well studied through the Stern-Volmer principle, which simplifies the effectiveness of a quenching material down to a single number, the Stern-Volmer quenching constant. By comparing the Stern-Volmer constants of various quenching materials and processes, one can easily tell which the most sensitive material is for a fluorescence-based sensor. In the case of our compound, as demonstrated in Figure 24, we can see that our polymeric system is most sensitive to picric acid, followed by TNT, DNT, and nitrobenzene. This is in line with our expectations based on our modeling in Figure, which predicted that the silicon center's Lewis acidity will attract more electronegative substituents. Further, the results summarized in Figure 24 show that our model was mostly accurate, correctly predicting that the 2,7 conjugated system is generally more sensitive than the 3,6 system. The results are summarized in Figure 25, shown above. While our polymeric system is less sensitive

Table 3: Stern-Volmer constants for the graphs shown in Figure 26, as well as the quality of the fit.

Best literature values added for comparison from Sohn et al[2]

| Analyte | Sample | Ksv (L/mol) | R^2 | intercept |
|---|---|---|---|---|
| PA | 2,7 | 84400 | 0.99 | 0.98 |
| | C | 43300 | 0.97 | 1.02 |
| | 3,6 | 46300 | 0.99 | 1.00 |
| | literature | 11000 | | |
| NB | 2,7 | 530 | 0.98 | 0.99 |
| | C | 452 | 0.98 | 0.98 |
| | 3,6 | 338 | 0.97 | 0.98 |
| | literature | 1230 | | |
| DNT | 2,7 | 861 | 0.99 | 0.98 |
| | C | 861 | 0.99 | 0.98 |
| | 3,6 | 1130 | 1.00 | 0.99 |
| | literature | 2570 | | |
| TNT | 2,7 | 1190 | 0.99 | 1.01 |
| | C | 2370 | 0.99 | 0.92 |
| | 3,6 | 1600 | 1.00 | 0.99 |
| | literature | 4340 | | |

than the previous literature sensors for TNT, DNT, and nitrobenzene, it is almost an order of magnitude more sensitive for picric acid, which is by far the most dangerous and the most toxic of all four compounds.[62] While picric acid has largely been replaced by more benign chemicals in industry, it is still used for some metallurgical applications under the trade name picral, as well as a fixative known as Bouin solution. Finally, munitions containing picric acid are still occasionally found in former war zones, from which it leaches into the surrounding environment.

2.1.6 Quenching mechanism

We believe that the quenching process for our polymer is static. This comes from several observations. First, there is no difference between the emission wavelengths of the polymeric system in different solvents. While this seems like an obvious observation, it does tell us that there is no exciplex formation during the fluorescence quenching process. Such an exciplex would have a solvent-dependent shift in fluorescence emission[63], as more polar solvents tend to favor a looser exciplex structure. The polar solvent solvates and stabilizes charge separation, preventing the stable exciplex from forming. This causes the emission wavelength to shift towards the component ions of the exciplex[64]. Exciplex formation would also be a form of dynamic quenching, as the exciplex forms only after the fluorophore is excited.

Next, we measured the fluorescence lifetime, $\tau$, and calculated $\frac{\tau_0}{\tau}$. This produced a flat line. Due to instrumental limitations, we could not measure the lifetime values for the 3,6-polyspirosilabifluorene system. This means that quencher concentration levels do not affect the quenching time, which would be necessary for a dynamic, collision-based, quenching process. Increased concentration of quencher would raise the number of

molecular collisions between the fluorophore and the quencher. Such collisional quenching would cause the plot of $\frac{\tau_0}{\tau}$ to be angled upwards with respect to quencher concentration. As we did not observe any change in fluorescence lifetime, we can conclude that a dynamic process is unlikely.

Finally, we could potentially try testing changes in fluorescence quenching at different temperatures. As dynamic quenching processes rely on collisions between molecules, while static quenching processes rely on complex formation, temperature would affect the Stern-Volmer constant very differently. Dynamic quenching would become more effective at higher temperatures, due to the increase in kinetic energy in the molecules causing more collisions. On the other hand, static quenching would become less efficient at higher temperatures, as the same increase in molecular kinetic energy would limit metastable complex formation. Such experiments were not carried out, as our instruments did not allow temperature control of the sample.

Modeling results have shown us that a trinitrobenzene molecule associates preferentially to a spirosilabifluorene dimer that is conjugated at the 2 and the 7 positions. This is further supported by HOMO/LUMO calculations, where the nodal plane of the HOMO passes through bonds in the 2, 7 conjugated system. The nodal planes of the 3, 6 conjugated system pass through a carbon atom, which causes a greater energy difference between the LUMO and the HOMO of the compound. Experimental evidence does not support this, however, as there is no discernable pattern in the Stern-Volmer constants shown in Table 3.

The results received were fitted according to the Stern-Volmer model described in Eq 2, consistent with only the presence of static quenching. Picric acid appears to be the

strongest quencher for the systems by far, likely caused by the strongly electronegative hydroxy group. This is in line with our expectations based on the models in Figure 11, which shows that the silicon atom seems to have a mildly Lewis acidic nature. This would attract the Lewis basic hydroxy group. The model is further confirmed by the 2,7 conjugated system with the silicon center being overall the most sensitive, with the 3,6 conjugated system being about even, or slightly less sensitive, when compared to the 2,7-carbon centered system.

Finally, the corrected Stern-Volmer plot showed us a quenching constant of approximately $8x10^5$ $M^{-1}$, which is nearly an order of magnitude more sensitive than current fluorescence based nitroaromatic sensors[65].

# CHAPTER 3: EXPERIMENTAL

Materials: o-dibromobenzene was used as received from Oakwood Chemical, 1,4-dibromo-2-nitrobenzene was used as obtained from TCI, and 2,2',7,7'-tetrabromospirobifluorene was used as obtained from Sigma Aldrich. Procedures were adapted from literature sources as well as a prior thesis.

Synthesis of **2,2'dibromobiphenyl**:[66]

o-dibromobenzene (5ml, 9.2g, 39.0mmol) was dissolved in 25ml of freshly distilled tetrahydrofuran (THF). The mixture was cooled to -80 $^{o}$C via acetone/LN2 slurry. n-BuLi (9ml, 2.5M, 22.5mmol) was added to the solution dropwise over 10 minutes under nitrogen atmosphere. The flask was kept cool for an additional hour, and then allowed to warm to room temperature and react overnight under $N_2$. The crude product was quenched with water and extracted with diethyl ether. The product was dried over sodium sulfate and the solvent was removed under vacuum, leaving behind white crystals. $^{1}$HNMR ($CDCl_3$, 300MHz) $\delta$ = 7.68 (d, 1H), 7.39 (d, 1H), 7.27 (t, 2H)

Synthesis of **4,4'-dibromo-2,2'-dinitrobiphenyl**:[66]

1,4-dibromo-2-nitrobenzene (3.12g, 11.1mmol) and copper powder (2.36g, 37.2mmol) were added to a round bottom flask under nitrogen atmosphere. 25ml of dry DMF was added to the flask. The solution was left to reflux for 3.5 hours, at which point 100ml of toluene was added and the mixture filtered through a celite plug. The filtrate was washed with water and brine, dried with sodium sulfate, and the solvent was removed under vacuum, leaving behind yellowish crystals. (1.89g, 84.5%) $^{1}$HNMR ($CDCl_3$, 300MHz) $\delta$ = 8.38 (d, 2H), 7.82 (d, 2H) 7.15 (s, 2H)

Synthesis of **4,4'-dibromo-2,2'-diaminobiphenyl**:[66]

4,4'-dibromo-2,2'-dinitrobiphenyl (0.686g, 1.7mmol) was added to a round bottom flask. 10ml of absolute ethanol was added to the flask. 10 ml of 37wt% HCl was added to the flask. Tin powder (1.42g, 12.0mmol) was added to the flask. The mixture was left to reflux for 3 hours. After reflux, the mixture was poured into an ice water slurry, and slowly quenched with NaOH until pH>10. The product was extracted with ether, dried over sodium sulfate, and solvent was removed under vacuum, resulting in a cream-colored powder. (0.436g, 75%) $^1$HNMR ($CDCl_3$, 300MHz) $\delta$ = 6.95 (s, 6H), 3.76 (s, 4H)

Synthesis of **4,4'-dibromo-2,2'-diiodobiphenyl**:[66]

4,4'-dibromo-2,2'-diaminobiphenyl (1.11g, 3.25mmol) was added to a flask containing 20ml acetonitrile (CAN), 20ml deionized water, and 10 ml 37wt% HCl. The mixture was cooled to -80 in a methanol/LN2 slurry, and sodium nitrite (1.28g, 18.6mmol) was added. The mixture was kept cold for one hour, and then potassium iodide (5.29g, 31.9mmol) was added. The mixture was warmed to 80 $^o$C and left to stir for 72 hours. The mixture was quenched with water and the product was extracted with diethyl ether. The organic layer was washed with a sodium dithionite solution, then dried over sodium sulfate and the solvent was removed under vacuum, leaving behind a dark red powder. (0.696g, 38%) $^1$HNMR ($CDCl_3$, 300MHz) $\delta$ = 8.1 (s, 2H), 7.56 (d, 2H), 7.03 (d, 2H)

Yamamoto coupling of **2,2',7,7' spirosilabifluorene**

2,2'-bipyridine was added to a flask under nitrogen atmosphere. Cyclooctadiene was added to the flask. Freshly opened anhydrous DMF was added to the flask. The flask was sparged with nitrogen for a half hour. Nickel cyclooctadiene was dissolved in dry DMF under nitrogen atmosphere. The two mixtures were mixed in a single flask under nitrogen. The resulting mixture was heated to 85 $^o$C for two hours. After heating, the

mixture was added to a flask containing 2,2',7,7' tetrabromospirosilabifluorene, and was allowed to stir at 85 $^{o}$C for 16 hours. The mixture was cooled in an ice bath and quenched with concentrated HCl. The solid product was removed by filtration and washed with DMF, water, and acetone 3x. Elemental analysis calculated range (%) for $C_{24}H_{16}Si$ – $C_{24}H_{12}Si$: C 86.70-87.77, H 4.85-3.68, Si:8.45-8.55, N 0; found (comb. anal.): C 80.9, H 4.4, N 0.0; found (EDAX): C 89.73, H ND, N 0.0, Si 6.42

Yamamoto coupling of **2,2',7,7' spirobifluorene**

2,2'-bipyridine was added to a flask under nitrogen atmosphere. Cyclooctadiene was added to the flask. Freshly opened anhydrous DMF was added to the flask. The flask was sparged with nitrogen for a half hour. Nickel cyclooctadiene was dissolved in dry DMF under nitrogen atmosphere. The two mixtures were mixed in a single flask under nitrogen. The resulting mixture was heated to 85 $^{o}$C for two hours. After heating, the mixture was added to a flask containing 2,2',7,7' tetrabromospirobifluorene, and was allowed to stir at 85 $^{o}$C for 16 hours. The mixture was cooled in an ice bath and quenched with concentrated HCl. The solid product was removed by filtration and washed with DMF, water, and acetone 3x. Elemental analysis calculated range (%) for $C_{25}H_{16}$ – $C_{25}H_{12}$: C 94.9-96.13, H 5.1-3.87, N 0; found (comb. anal.): C 93.1, H 4.5, N 0.4; found (EDAX): C 95.89, H ND, N ND

Yamamoto coupling of **3,3',6,6' spirosilabifluorene**

2,2'-bipyridine was added to a flask under nitrogen atmosphere. Cyclooctadiene was added to the flask. Freshly opened anhydrous DMF was added to the flask. The flask was sparged with nitrogen for a half hour. Nickel cyclooctadiene was dissolved in dry DMF under nitrogen atmosphere. The two mixtures were mixed in a single flask under

nitrogen. The resulting mixture was heated to 85 $^{o}$C for two hours. After heating, the mixture was added to a flask containing 3,3',6,6' tetrabromospirosilabifluorene, and was allowed to stir at 85 $^{o}$C for 16 hours. The mixture was cooled in an ice bath and quenched with concentrated HCl. The solid product was removed by filtration and washed with DMF, water, and acetone 3x. Elemental analysis calculated range (%) for $C_{24}H_{16}Si$ – $C_{24}H_{12}Si$:C 86.70-87.77, H 4.85-3.68, Si:8.45-8.55, N 0; found (comb. anal.): C 81.8, H 4.4, N 0.4; found (EDAX): C 88.85, H ND, N ND, Si 6.76

# CHAPTER 4: CONCLUSIONS AND FUTURE DIRECTIONS

Overall, we successfully demonstrated that tetrabromosilaspirobifluorenes are a stable building block for condensed polymeric networks generated via Yamamoto coupling. The 3,6 silaspirobifluorene system offers a somewhat unique geometry that is not straightforward to create with a carbon centered spirobifluorene system. As the 2,7 system is significantly stabilized when compared to the 3,6 system, it is impossible to generate the carbon centered 3,6 system without using a roundabout synthetic method. This material also has extreme thermal stability and very high surface area. This makes it an attractive platform for future heteropolymeric networks.

We also showed that modeling of the polymer system is both easy and reliable. We were able to accurately predict the different optical properties of our polymer systems and confirm them experimentally. This was shown to occur due to the difference in delocalization of the HOMO/LUMO between the two polymer morphologies, with the 2,7-system stabilized when compared to the 3,6-system. The LUMO of the 3,6 system has nodal planes passing through the carbon atoms that make up part of the ring, while the 2,7 system allows the nodal planes to pass through the bonds. This is the reason for both the increased stability of the 2,7-system, and why it is easier to synthesize the 2,7-system when starting with a spirobifluorene.

Additionally, we demonstrated that the spirobifluorene network is an attractive sensor for nitroaromatics based on a static fluorescence quenching process. This is promising, as the high energy blue emission can be tuned through the addition of various struts or copolymers to change the sensor targets. The current polymer system shows negligible solubility, which is both a positive and a negative depending on the sensing

application. However, we expect that a system containing longer struts would be more soluble in comparison, and through proper strut management could be used to tune the properties of the polymer to the point of selective solubility as well as selective fluorescence emissions and sensing. One possible drawback is the potential to lose both porosity and the high surface area of the polymer, as the new struts would allow more flexibility in the polymer chain. As the porosity and surface area is currently dictated by the rigid spiro-linkages and the extended conjugation present in the polymer, adding longer struts would likely allow the polymer to fold in on itself more efficiently than is possible with the currently studied morphology.

Finally, we showed that the Lewis acidity of the silicon atom is not a significant factor when it comes to fluorescence quenching, which was somewhat surprising. The carbon centered polymer had similar performance to the silicon centered analog in respect to quenching, with no clear advantage to either system. While this is not an important distinction for the quenching process, the silaspirobifluorene polymer is easier to modify at the 3,6 position, which makes it an attractive prospect for generating novel structural motifs within polymers. Considering the difference in the HOMO between the 3,6 and the 2,7 systems, this is potentially a useful direction for future research that focuses on exploiting this property specifically.

## REFERENCES


(1) Sanchez, J. C., UCSD, 2008.

(2) Sohn, H.; Sailor, M. J.; Magde, D.; Trogler, W. C. *Journal of the American Chemical Society* **2003**, *125*, 3821.

(3) Mazaj, M.; Volkringer, C.; Loiseau, T.; Kaučič, V.; Férey, G. *Solid State Sciences* **2011**, *13*, 1488.

(4) Notario, B.; Pinto, J.; Rodriguez-Perez, M. A. *Progress in Materials Science* **2016**, *78-79*, 93.

(5) Cichosz, S.; Masek, A.; Zaborski, M. *Polymer Testing* **2018**, *67*, 342.

(6) Tran, Y. T.; Lee, J.; Kumar, P.; Kim, K.-H.; Lee, S. S. *Composites Part B: Engineering* **2019**, *165*, 354.

(7) Cychosz, K. A.; Thommes, M. *Engineering* **2018**, *4*, 559.

(8) Dehghan, R.; Anbia, M. *Fuel Processing Technology* **2017**, *167*, 99.

(9) Feliczak-Guzik, A. *Microporous and Mesoporous Materials* **2018**, *259*, 33.

(10) Ch. Baerlocher, L. B. M.

(11) Shi, Z.; Zhang, Y.; Phillips, G. O.; Yang, G. *Food Hydrocolloids* **2014**, *35*, 539.

(12) Aboelnaga, A.; Elmasry, M.; Adly, O. A.; Elbadawy, M. A.; Abbas, A. H.; Abdelrahman, I.; Salah, O.; Steinvall, I. *Burns* **2018**, *44*, 1982.

(13) Vogt, E. T. C.; Weckhuysen, B. M. *Chemical Society Reviews* **2015**, *44*, 7342.

(14) Davis, M. E. *Nature* **2002**, *417*, 813.

(15) Mintova, S.; Jaber, M.; Valtchev, V. *Chemical Society Reviews* **2015**, *44*, 7207.

(16) Dusselier, M.; Van Wouwe, P.; Dewaele, A.; Jacobs, P. A.; Sels, B. F. *Science* **2015**, *349*, 78.

(17) Pacheco, J. J.; Davis, M. E. *Proceedings of the National Academy of Sciences* **2014**, *111*, 8363.

(18) Dijkmans, J.; Dusselier, M.; Gabriëls, D.; Houthoofd, K.; Magusin, P. C. M. M.; Huang, S.; Pontikes, Y.; Trekels, M.; Vantomme, A.; Giebeler, L.; Oswald, S.; Sels, B. F. *ACS Catalysis* **2015**, *5*, 928.

(19) Wang, C.; Wang, L.; Zhang, J.; Wang, H.; Lewis, J. P.; Xiao, F.-S. *Journal of the American Chemical Society* **2016**, *138*, 7880.

(20) Dawson, R.; Cooper, A. I.; Adams, D. J. *Progress in Polymer Science* **2012**, *37*, 530.

(21) Mehtab, T.; Yasin, G.; Arif, M.; Shakeel, M.; Korai, R. M.; Nadeem, M.; Muhammad, N.; Lu, X. *Journal of Energy Storage* **2019**, *21*, 632.

(22) Farha, O. K.; Eryazici, I.; Jeong, N. C.; Hauser, B. G.; Wilmer, C. E.; Sarjeant, A. A.; Snurr, R. Q.; Nguyen, S. T.; Yazaydın, A. Ö.; Hupp, J. T. *Journal of the American Chemical Society* **2012**, *134*, 15016.

(23) Kutzscher, C.; Nickerl, G.; Senkovska, I.; Bon, V.; Kaskel, S. *Chemistry of Materials* **2016**, *28*, 2573.

(24) Segura, J. L.; Mancheño, M. J.; Zamora, F. *Chemical Society Reviews* **2016**, *45*, 5635.

(25) Wang, K.; Qi, D.; Li, Y.; Wang, T.; Liu, H.; Jiang, J. *Coordination Chemistry Reviews* **2019**, *378*, 188.

(26) Cooper, A. I. **2009**, *21*, 1291.

(27) Ding, S.-Y.; Wang, W. *Chemical Society Reviews* **2013**, *42*, 548.

(28) Tan, L.; Tan, B. *Chemical Society Reviews* **2017**, *46*, 3322.

(29) Li, X.; Chen, G.; Ma, J.; Jia, Q. *Separation and Purification Technology* **2019**, *210*, 995.

(30) Xu, F.; Wu, D.; Fu, R.; Wei, B. *Materials Today* **2017**, *20*, 629.

(31) Wang, Z. J.; Li, R.; Landfester, K.; Zhang, K. A. I. *Polymer* **2017**, *126*, 291.

(32) Wu, D.; Xu, F.; Sun, B.; Fu, R.; He, H.; Matyjaszewski, K. *Chemical Reviews* **2012**, *112*, 3959.

(33) McKeown, N. B. *ISRN Materials Science* **2012**, *2012*, 16.

(34) McKeown, N. B. *Science China Chemistry* **2017**, *60*, 1023.

(35) Long, T. M.; Swager, T. M. *Advanced Materials* **2001**, *13*, 601.

(36) Ramimoghadam, D.; Gray, E. M.; Webb, C. J. *International Journal of Hydrogen Energy* **2016**, *41*, 16944.

(37) Ramakrishna, J.; Venkatakrishnan, P. *Chemistry – An Asian Journal* **2017**, *12*, 181.

(38) Xie, Z.; Wei, Y.; Zhao, X.; Li, Y.; Ding, S.; Chen, L. *Materials Chemistry Frontiers* **2017**, *1*, 867.

(39) Krishna, A.; Sabba, D.; Yin, J.; Bruno, A.; Antila, L. J.; Soci, C.; Mhaisalkar, S.; Grimsdale, A. C. *Journal of Materials Chemistry A* **2016**, *4*, 8750.

(40) Xiao, H.; Leng, B.; Tian, H. *Polymer* **2005**, *46*, 5707.

(41) Wolfe, J. P.; Singer, R. A.; Yang, B. H.; Buchwald, S. L. *Journal of the American Chemical Society* **1999**, *121*, 9550.

(42) Tanaka, N.; Mizoshita, N.; Maegawa, Y.; Tani, T.; Inagaki, S.; Jorapur, Y. R.; Shimada, T. *Chemical Communications* **2011**, *47*, 5025.

(43) Kuninobu, Y.; Yamauchi, K.; Tamura, N.; Seiki, T.; Takai, K. *Angewandte Chemie International Edition* **2013**, *52*, 1520.

(44) Wang, D.; Liu, Q.; Yu, Y.; Wu, Y.; Zhang, X.; Dong, H.; Ma, L.; Zhou, G.; Jiao, B.; Wu, Z.; Chen, R. *Science China Chemistry* **2015**, *58*, 993.

(45) Sanchez, J. C.; Trogler, W. C. *Journal of Materials Chemistry* **2008**, *18*, 3143.

(46) Hogarth, C. W. **1912**, *1*, 183.

(47) Caskey, D. C.; Chapman, D. W. 1983.

(48) Koskin, A. P.; Kenzhin, R. V.; Vedyagin, A. A.; Mishakov, I. V. *Catalysis Communications* **2014**, *53*, 83.

(49) Furman, D.; Kosloff, R.; Dubnikova, F.; Zybin, S. V.; Goddard, W. A.; Rom, N.; Hirshberg, B.; Zeiri, Y. *Journal of the American Chemical Society* **2014**, *136*, 4192.

(50) Ju, K.-S.; Parales, R. E. **2010**, *74*, 250.

(51) Venkatramaiah, N.; Pereira, C. F.; Mendes, R. F.; Paz, F. A. A.; Tomé, J. P. C. *Analytical Chemistry* **2015**, *87*, 4515.

(52) Mullen, C.; Irwin, A.; Pond, B. V.; Huestis, D. L.; Coggiola, M. J.; Oser, H. *Analytical Chemistry* **2006**, *78*, 3807.

(53) Oxley, J. C.; Waggoner, L. P. In *Aspects of Explosives Detection*; Marshall, M., Oxley, J. C., Eds.; Elsevier: Amsterdam, 2009, p 27.

(54) Yinon, J. *Analytical Chemistry* **2003**, *75*, 98 A.

(55) Swager, T. M. *Accounts of Chemical Research* **2008**, *41*, 1181.

(56) Schmidt, J.; Werner, M.; Thomas, A. *Macromolecules* **2009**, *42*, 4426.

(57) Tamao, K.; Uchida, M.; Izumizawa, T.; Furukawa, K.; Yamaguchi, S. *Journal of the American Chemical Society* **1996**, *118*, 11974.

(58) Lee, S. H.; Jang, B.-B.; Kafafi, Z. H. *Journal of the American Chemical Society* **2005**, *127*, 9071.

(59) Hauser, B. G.; Farha, O. K.; Exley, J.; Hupp, J. T. *Chemistry of Materials* **2013**, *25*, 12.

(60) Thommes, M.; Kaneko, K.; Neimark Alexander, V.; Olivier James, P.; Rodriguez-Reinoso, F.; Rouquerol, J.; Sing Kenneth, S. W. In *Pure and Applied Chemistry* 2015; Vol. 87, p 1051.

(61) Ismail, I. M. K. *Langmuir* **1992**, *8*, 360.

(62) US National Library of Medicine: Hazardous Substances Data Bank, 2018.

(63) Bichenkova, E. V.; Sardarian, A. R.; Wilton, A. N.; Bonnet, P.; Bryce, R. A.; Douglas, K. T. *Organic & Biomolecular Chemistry* **2006**, *4*, 367.

(64) Orbach, N.; Ottolenghi, M. *Chemical Physics Letters* **1975**, *35*, 175.

(65) Shanmugaraju, S.; Joshi, S. A.; Mukherjee, P. S. *Journal of Materials Chemistry* **2011**, *21*, 9130.

(66) Lee, D., UNCC, 2015.

**Figure 1** By Robneild at en.wikipedia, CC BY-SA 3.0,

**Figure 2** By Lenntech